

# SCONCE: A cosmic web finder for spherical and conic geometries

Yikun Zhang,<sup>1</sup>\* Rafael S. de Souza,<sup>2</sup>† and Yen-Chi Chen<sup>1</sup>‡

<sup>1</sup>*Department of Statistics, University of Washington, Seattle, WA 98195, United States*

<sup>2</sup>*Key Laboratory for Research in Galaxies and Cosmology, Shanghai Astronomical Observatory, Chinese Academy of Sciences, Shanghai 200030, China*

Accepted XXX. Received YYY; in original form ZZZ

## ABSTRACT

The latticework structure known as the cosmic web provides a valuable insight into the assembly history of large-scale structures. Despite the variety of methods to identify the cosmic web structures, they mostly rely on the assumption that galaxies are embedded in a Euclidean geometric space. Here we present a novel cosmic web identifier called SCONCE (Spherical and CONic Cosmic wEb finder) that inherently considers the 2D (RA,DEC) spherical or the 3D (RA,DEC,z) conic geometry. The proposed algorithms in SCONCE generalize the well-known subspace constrained mean shift (SCMS) method and primarily address the predominant filament detection problem. They are intrinsic to the spherical/conic geometry and invariant to data rotations. We further test the efficacy of our method with an artificial cross-shaped filament example and apply it to the SDSS galaxy catalogue, revealing that the 2D spherical version of our algorithms is robust even in regions of high declination. Finally, using N-body simulations from Illustris, we show that the 3D conic version of our algorithms is more robust in detecting filaments than the standard SCMS method under the redshift distortions caused by the peculiar velocities of halos. Our cosmic web finder is packaged in python as SCONCE-SCMS and has been made publicly available.

**Key words:** methods: data analysis – methods: statistical – cosmology: observations – large- scale structure of Universe.

## 1 INTRODUCTION

The cosmic web, a latticework structure of magnificent proportions, represents one of the most prominent physical patterns in the Universe (Bond et al. 1996). Its network nature is a byproduct of the hierarchical growth of large-scale structures of the Universe, which have been corroborated by observations of large-scale surveys (Ivezić et al. 2019; Abdurro’uf et al. 2021) and cosmological N-body simulations (Springel et al. 2005; Vogelsberger et al. 2014a). The structure is composed of a network of galaxy groups and clusters, filaments, sheets, and the large regions of near-emptiness known as cosmic voids (Zeldovich et al. 1982). In particular, the filamentary part of the cosmic web, as traced by galaxies, has been observed by several galaxy surveys, including the Sloan Digital Sky Survey (SDSS; York et al. 2000), the two degree Field Galaxy Redshift Survey (2dFGRS; Colless et al. 2003), the Cosmic Evolution Survey (COSMOS; Scoville et al. 2007), the VIMOS VLT deep survey (Le Fèvre et al. 2005), the 6dF Galaxy Survey (6dFGS; Jones et al. 2009), the Galaxy and Mass Assembly (GAMA; Driver et al. 2011), VIPERS (Guzzo et al. 2014) and SAMI (Bryant et al. 2015).

As the baryonic matter distribution correlates – to a certain extent – with the distribution of dark matter, galaxy properties are expected to correlate to their environment and, as such, to the local properties of the cosmic web. Filaments are known to be correlated with the stellar masses, intrinsic alignments, and luminosity of nearby galaxies (Zhang et al. 2013; Clampitt et al. 2016; Poudel et al. 2017; Chen

et al. 2017, 2019). For instance, the filament between clusters Abell 0399 and 0401 has been shown to host quiescent galaxies and hot gas and to emit in radio (Bonjean et al. 2018; Govoni et al. 2019). Darvish et al. (2014) suggested that mild galaxy-galaxy interactions play a role in increasing the fraction of H $\alpha$  star-forming galaxies in filaments. Using spectroscopic data from the main galaxy sample of the SDSS data release 7 (Abazajian et al. 2009), Kraljic et al. (2020) found that galaxy properties such as stellar mass, star formation activity, and morphology display some degree of dependence on the connectivity of the cosmic web.

Detection of filaments in a large volume has recently been carried out by Malavasi et al. (2020), using galaxy samples from SDSS (York et al. 2000), while Galárraga-Espinosa et al. (2020) applies a similar approach to hydrodynamical simulations to derive the expected statistical properties of filaments. There are several reasons why we are mainly interested in identifying one-dimensional cosmic filaments. Methodologically, detecting the filaments is relatively more robust than identifying cosmic sheets, whose tenuous structures may have low signal-to-noise ratios. Furthermore, filaments connect those zero-dimensional galaxy clusters and circumvent the empty cosmic voids. Any precise filament detection method can infer the locations of cosmic voids by outlining their boundaries, which provides rich resources to infer the cosmology (Kreisch et al. 2021). Diving deeper into this vein, filaments also provide information about the nature of dark matter halos (Aragón-Calvo et al. 2007b; Zhang et al. 2009).

Despite the undoubtedly role of cosmic filaments in galaxy formation, identifying them on either observed or simulated galaxy distributions is challenging due to their intricate geometrical patterns (see, e.g. Cautun et al. 2014; Libeskind et al. 2018, for a detailed re-

\* E-mail: yikun@uw.edu

† E-mail: drsouza@shao.ac.cn

‡ E-mail: yenchi@uw.edu

view). Some filament finders in the literature span from investigating the Hessian matrix of the matter/galaxy density function: Skeleton (Novikov et al. 2006), Multiscale Morphology Filter (Aragón-Calvo et al. 2007a), NEXUS (Cautun et al. 2013), COWS (Pfeifer et al. 2022) to directly segmenting the density function via some topological principles: SpineWeb (Aragón-Calvo et al. 2010b), DisPerSE (Sousbie 2011; Sousbie et al. 2011).

In this work, we present a novel cosmic web finder that is adaptive to the spherical and light-cone geometries by generalizing the classical subspace constrained mean shift (SCMS) algorithm (Ozertem & Erdogmus 2011) and its prototypical mean shift algorithm (Comaniciu & Meer 2002). SCMS has been used in astronomy to identify cosmic filaments as density ridges (Chen et al. 2015b,c, 2016; Hendel et al. 2019; Moews et al. 2021b; Carrón Duque et al. 2022). Our first generalization extends upon these past implementations and is more accurate in recovering cosmic web structures on the celestial sphere indicated by the (RA,DEC) coordinate system, especially in regions of higher declination. Our second generalization further extends our new SCMS method to a 3D light cone specified by the (RA,DEC, $z$ ) coordinate system. In essence, the Spherical and CONic Cosmic web finder (SCONCE) estimates the matter/galaxy density function on the celestial sphere or the 3D light cone based on the Cartesian representation of (RA,DEC). Such a density function on the sphere (or 3D light cone) is known as the directional (or directional-linear) density in Statistics (Mardia & Jupp 2000; Ley & Verdebout 2017; Pewsey & García-Portugués 2021). For a given estimated matter density function on the sphere or spherical cone, SCONCE recovers the filaments as the density ridges of the estimated density via adaptive gradient ascent iterations (Zhang & Chen 2021d; Zhang & Chen 2021b,c).

This paper is organized as follows. Section 2 reviews the standard SCMS algorithm and describes our extensions on the spherical and conic geometries. Applications to mock and real-world astronomical data are presented at Section 3, including comparisons with the other SCMS typed and DisPerSE algorithms. Finally, Section 4 provides our summary and discussion. Throughout this work, we assume a Wilkinson Microwave Anisotropy Probe (WMAP)-9 cosmology ( $\Omega_m = 0.2726$ ,  $\Omega_b = 0.0456$ ,  $\Omega_\Lambda = 0.7274$ , and  $h = 0.704$ ; Hinshaw et al. 2013).

## 2 METHODOLOGY

This section describes the general aspects of the standard SCMS algorithm in the Euclidean space and our extended SCMS algorithms in SCONCE. The extensions enable better characterizations of the density ridges (*i.e.*, our filament model) and their associated nodes according to a collection of discrete observations on the celestial sphere

$$\mathbb{S}^2 = \left\{ \mathbf{x} \in \mathbb{R}^3 : \|\mathbf{x}\|_2 = 1 \right\} \simeq \{(\alpha, \delta) \in [0^\circ, 360^\circ) \times [-90^\circ, 90^\circ] : \alpha \text{ is RA and } \delta \text{ is DEC}\},$$

or the 3D light cone  $\mathbb{S}^2 \times \mathbb{R}$ . Here,  $\simeq$  stands for the equivalent representation,  $\mathbb{R}$  is the real line, and  $\|\cdot\|_2$  is the Euclidean norm. SCONCE has been made publicly available<sup>1</sup> and can be installed via pip command.

### 2.1 SCMS Algorithm on the Euclidean Space $\mathbb{R}^d$

Introduced by Ozertem & Erdogmus (2011), the standard SCMS algorithm is part of the taxonomy of statistical methods dealing with the

estimation of local principal curves, more widely known as density ridges (Eberly 1996; Genovese et al. 2014; Chen et al. 2015a) in the flat Euclidean space  $\mathbb{R}^d$ . Suppose we start with a mesh of points placed in equidistant steps across the data space. In that case, the algorithm seeks to establish density ridges in an iterative process resembling the gradient ascent method. The procedure can be visualized as a cloud of points shifting closer to the nearest underlying structure at each iteration.

#### 2.1.1 Filament Model in $\mathbb{R}^d$

Formally speaking, a density ridge is the maximization of the local density in the normal direction defined by the Hessian matrix. Let  $\nabla p(\mathbf{x})$  be the gradient of a probability density function  $p$  on a  $d$ -dimensional Euclidean space  $\mathbb{R}^d$ , and  $H(\mathbf{x}) \equiv \nabla \nabla p(\mathbf{x})$  be its Hessian matrix of second derivatives, whose orthonormal eigenvectors  $\mathbf{v}_1(\mathbf{x}), \dots, \mathbf{v}_d(\mathbf{x})$  are associated with a descending order of eigenvalues  $\lambda_1(\mathbf{x}) \geq \dots \geq \lambda_d(\mathbf{x})$ . The density ridge of  $p$  is defined as the collection of points satisfying

$$R(p) = \left\{ \mathbf{x} \in \mathbb{R}^d : V_E(\mathbf{x})^T \nabla p(\mathbf{x}) = \mathbf{0}, \lambda_2(\mathbf{x}) < 0 \right\}, \quad (1)$$

where  $V_E(\mathbf{x}) = [\mathbf{v}_2(\mathbf{x}), \dots, \mathbf{v}_d(\mathbf{x})] \in \mathbb{R}^{d \times (d-1)}$  has its columns composed by all but the first eigenvector of the Hessian  $H(\mathbf{x})$ . In principle, the density function  $p$  is distinctively curved along the space defined by the columns of  $V_E(\mathbf{x})$ , within which  $R(p)$  consists of its local maxima. The density ridge  $R(p)$  serves as a theoretical cosmic filament model in  $\mathbb{R}^d$  with an arbitrary dimension  $d$ .

#### 2.1.2 Filament Estimation in $\mathbb{R}^d$ : The Standard SCMS Algorithm

To approximate the theoretical density ridge (1), a common strategy is to use the density ridge  $\hat{R} \equiv R(\hat{p})$  defined by the kernel density estimator (KDE)  $\hat{p}$ . Given some observations  $X_1, \dots, X_n \subset \mathbb{R}^d$  from  $p$ , the KDE  $\hat{p}$  estimates the density function as:

$$\hat{p}(\mathbf{x}) = \frac{1}{nb^d} \sum_{i=1}^n K \left( \left\| \frac{\mathbf{x} - X_i}{b} \right\| \right), \quad (2)$$

where  $K(\cdot)$  is a kernel function<sup>2</sup> and  $b$  is the smoothing bandwidth parameter (see, e.g., Scott 2015; Chen 2017, for more details about the choices of  $K(\cdot)$  and  $b$ ). Commonly, a larger value of  $b$  leads to a smoother  $\hat{p}$  and a less intricate density ridge  $R(\hat{p})$ . The standard SCMS algorithm iterates an initial mesh of points along the direction of the (estimated) projected gradient  $\hat{V}_E(\mathbf{x}) \hat{V}_E(\mathbf{x})^T \nabla \hat{p}(\mathbf{x})$  defined by the KDE  $\hat{p}$  until convergence (see, e.g., Algorithm 1 in Zhang & Chen (2021b) for the full formulation). Unlike the ordinary gradient ascent method, which requires some delicate choices of the step size parameter, the SCMS and its prototypical mean shift algorithms embrace an adaptive step size with respect to the data and bandwidth parameter  $b$ . As long as  $b$  is reasonably small, the mean shift and SCMS algorithms are guaranteed to converge (Cheng 1995; Li et al. 2007; Arias-Castro et al. 2016; Aliyari Ghassabeh et al. 2013; Zhang & Chen 2021b). The set of converged points under the SCMS algorithm becomes a discrete sample from the density ridge  $R(\hat{p})$ .

Despite its broad applicability in detecting filamentary structures (Chen et al. 2015c; Fernandez et al. 2020; Chen et al. 2020), the standard SCMS algorithm has shortcomings when the curvature where the

<sup>1</sup> The code is available at <https://pypi.org/project/sconce-scms/>.

<sup>2</sup> For instance, the Gaussian kernel  $K(r) = \frac{1}{(2\pi)^{d/2}} \exp\left(-\frac{r^2}{2}\right)$ .

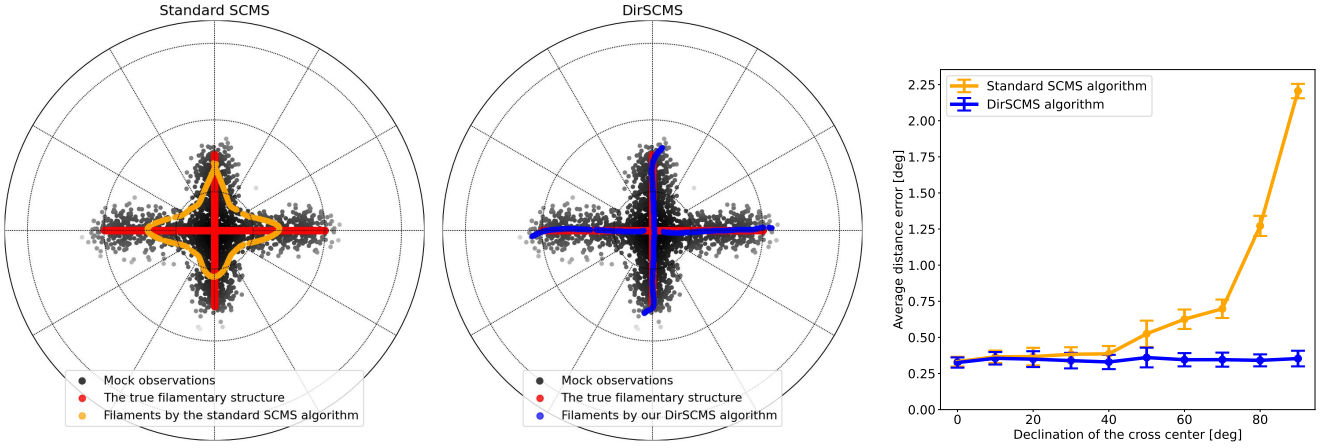


**Figure 1.** Comparisons between the standard SCMS and our extended DirSCMS algorithms applied to the mock dataset on  $\mathbb{S}^2$ . The *left* and *middle* panels depict the mock observations, true cross-shaped filament, and the estimated filaments yielded by the standard SCMS and our DirSCMS algorithms, respectively. The *right* panel presents the average distance errors from the estimated filaments yielded by the standard SCMS and our DirSCMS algorithms to the true filaments as we varies the declination values on which the true filament centers.

data live is non-negligible, which may produce highly biased estimates of the cosmic web. To showcase this effect, we create a simple experiment. Starting from a cross-shaped filamentary structure with its center at the North pole of the sphere  $\mathbb{S}^2$ , we generate a mock dataset consisting of 2,000 mock observations from the true filament with independent Gaussian noises of zero mean and 0.05 standard deviation (see Figure 1). We then apply both the standard SCMS and our extended DirSCMS method (Section 2.2.2) in order to recover the original cross-shaped structure. A visual inspection of Figure 1 reveals that the standard SCMS algorithm fails to approximate the true filamentary structure near the North pole (*i.e.*, the center of the cross). On the contrary, our DirSCMS method manages to recover the entire cross-shaped filament.<sup>3</sup> To further quantify how the location of the true filament would influence each algorithm’s estimate, we generate the same experiment several times but with different declination values for the center of the true filament, spanning from  $0^\circ$  to  $90^\circ$ . For each declination, we compute the average distance errors from the estimated filaments detected by the standard SCMS and our DirSCMS algorithms to the true cross-shaped filament on  $\mathbb{S}^2$ , respectively. Results are shown on the right panel of Figure 1. The error bars indicate the standard deviations of the average distance errors, which are obtained by repeating the data sampling and filament detection procedure 20 times. This toy experiment suggests that our DirSCMS algorithm outperforms the standard SCMS algorithm when the filamentary structures are located at the regions with declination higher than  $50^\circ$ . More importantly, the estimation bias of our DirSCMS algorithm is invariant under translations on  $\mathbb{S}^2$ .

## 2.2 SCMS Algorithm on the Celestial Sphere $\mathbb{S}^2$

To address the estimation bias of the standard SCMS algorithm in the regions of high declination on the (unit) celestial sphere  $\mathbb{S}^2$ , we introduce our first SCMS extension to tackle the spherical geometry. We consider  $n$  observations with their angular coordinates as  $(\alpha_i, \delta_i) \in [0, 360^\circ) \times [-90^\circ, 90^\circ]$  for  $i = 1, \dots, n$ , where  $\alpha_i$  is the right ascension (RA) of the  $i$ -th object and  $\delta_i$  is its declination (DEC).

<sup>3</sup> We selected the bandwidth parameters for the standard SCMS and our DirSCMS algorithms via Equations (13) and (14) with  $A_0 = 1.25$  and  $B_0 = 1$ . The results in Figure 1 are similar under other choices of the parameters.

Note that both Moews et al. (2021b) and Carrón Duque et al. (2022) have considered estimating the matter/galaxy density function (as well as its gradient and Hessian fields) under the geodesic distance on the (RA, DEC) angular coordinate system of  $\mathbb{S}^2$ , by leveraging either the haversine formula (Inman 1849) or the Hierarchical Equal Area isoLatitude Pixelisation (HEALPix; Górski et al. 2005) scheme. While their approaches reduce the bias in density estimation on the sphere, the subsequent SCMS iterations fail to converge to the (true) filamentary structures at the regions of high declination. Moreover, given the anisotropy of the (RA, DEC) angular coordinate system between regions of low and high declination, the SCMS algorithm based on this coordinate system is not completely invariant to the data rotation on  $\mathbb{S}^2$ .

### 2.2.1 Filament Model on $\mathbb{S}^2$

Different from how Moews et al. (2021b) and Carrón Duque et al. (2022) handle the spherical geometry, we convert the (RA, DEC) coordinates of the  $n$  observations to their Cartesian representations  $X_1, \dots, X_n$  on the (unit) sphere  $\mathbb{S}^2$  as:

$$X_i = (\cos \delta_i \cos \alpha_i, \cos \delta_i \sin \alpha_i, \sin \delta_i) \quad \text{for } i = 1, \dots, n. \quad (3)$$

We assume that  $X_1, \dots, X_n$  are random observations sampled from a (directional) density function  $f$  on  $\mathbb{S}^2$ . The filaments are modeled as the one-dimensional (directional) density ridge of  $f$  on  $\mathbb{S}^2$ . Mathematically, a (directional) density ridge  $R(f)$  is defined through the Riemannian gradient  $\text{grad } f(\mathbf{x})$  and Riemannian Hessian matrix  $\mathcal{H}f(\mathbf{x})$  on  $\mathbb{S}^2$ ; see Appendix A for their detailed expressions. Let  $\mathbf{v}_1(\mathbf{x}), \mathbf{v}_2(\mathbf{x})$  be the orthonormal eigenvectors of  $\mathcal{H}f(\mathbf{x})$  that lie within the tangent space  $T_{\mathbf{x}}$  at  $\mathbf{x} \in \mathbb{S}^2$  and  $\lambda_1(\mathbf{x}) \geq \lambda_2(\mathbf{x})$  be their associated eigenvalues.<sup>4</sup> Then, the (directional) density ridge  $R(f)$  on  $\mathbb{S}^2$  is the set of points satisfying

$$R(f) = \left\{ \mathbf{x} \in \mathbb{S}^2 : \mathbf{v}_2(\mathbf{x})^T \text{grad } f(\mathbf{x}) = 0, \lambda_2(\mathbf{x}) < 0 \right\}. \quad (4)$$

In contrast to the classical definition of density ridges in flat Euclidean spaces (Eberly 1996; Genovese et al. 2014; Chen et al. 2015a),

<sup>4</sup> Notice that  $\mathbf{v}_1(\mathbf{x}), \mathbf{v}_2(\mathbf{x})$  span the two-dimensional tangent space  $T_{\mathbf{x}}$ , and the Riemannian Hessian matrix  $\mathcal{H}f(\mathbf{x})$ , by definition, has another unit eigenvector  $\mathbf{x}$  that is orthogonal to  $T_{\mathbf{x}}$  associated with eigenvalue 0.

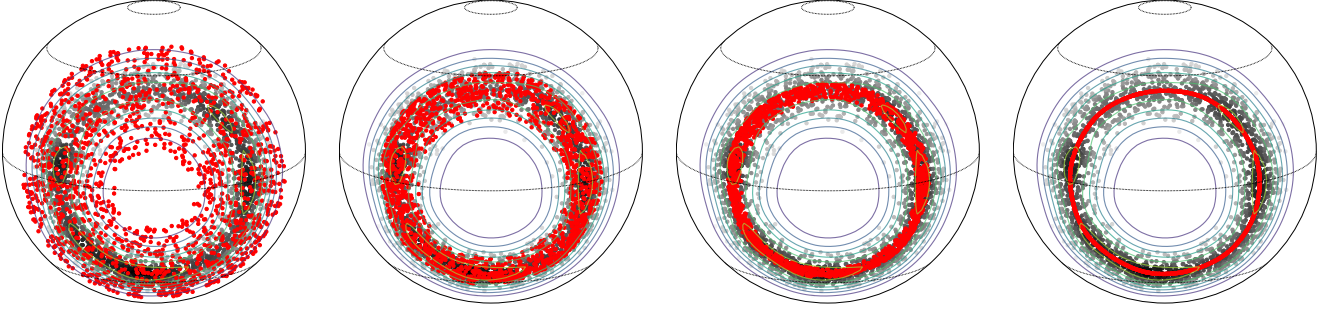


**Figure 2.** Step-by-step illustrations of our DirSCMS algorithm on  $\mathbb{S}^2$ . We sample some uniform mesh points (red dots) covering the input observations (gray dots) and apply our DirSCMS algorithm to the mesh points. The panels from left to right present the DirSCMS iteration at step 0, 1, 2, and 8. The contour lines in each panel indicate the directional KDE (5) applied to the input observations under their Cartesian coordinates  $\mathbf{X}_1, \dots, \mathbf{X}_n \subset \mathbb{S}^2$ .

our (directional) density ridge  $R(f)$  is defined through the (intrinsic/Riemannian) gradient and Hessian of  $f$  within the tangent spaces of  $\mathbb{S}^2$ . As a result, this filament model on  $\mathbb{S}^2$  is, by nature, adaptive to the spherical geometry and invariant to any rotation (*i.e.*, isotropic) in the (RA,DEC) space.

### 2.2.2 Filament Estimation on $\mathbb{S}^2$ : Directional SCMS Algorithm

To identify the density ridge (4) from  $n$  observations on  $\mathbb{S}^2$  with Cartesian coordinates  $\{\mathbf{X}_1, \dots, \mathbf{X}_n\} \subset \mathbb{S}^2$ , we first estimate the (directional) density function  $f$  through the directional KDE (Hall et al. 1987; Bai et al. 1988; Zhao & Wu 2001; García-Portugués 2013) as:

$$\hat{f}(\mathbf{x}) = \frac{C_L(b)}{n} \sum_{i=1}^n L\left(\frac{1 - \mathbf{x}^T \mathbf{X}_i}{b^2}\right), \quad (5)$$

where  $L(\cdot)$  is a directional kernel function (*e.g.*, the von Mises kernel  $L(r) = e^{-r}$ ),  $b$  is the smoothing bandwidth parameter, and  $C_L(b)$  is a normalizing constant ensuring that the integration of  $\hat{f}$  on  $\mathbb{S}^2$  is one. The choice of smoothing bandwidth parameter  $b$  is a critical factor in determining the performance of the estimator (5) and its density ridge filament model. Several statistical papers have been addressing the bandwidth selection problem (Hall et al. 1987; Taylor 2008; Oliveira et al. 2012; García-Portugués 2013; Saavedra-Nieves & María Crujeiras 2020), so we omit a detailed discussion here.

Given the directional KDE (5), our practical filament model on  $\mathbb{S}^2$  is given by a plug-in estimator of the theoretical one  $R(f)$  as:

$$R(\hat{f}) = \left\{ \mathbf{x} \in \mathbb{S}^2 : \hat{\mathbf{v}}_2(\mathbf{x})^T \text{grad } \hat{f}(\mathbf{x}) = 0, \hat{\lambda}_2(\mathbf{x}) < 0 \right\}, \quad (6)$$

where  $\hat{\mathbf{v}}_2(\mathbf{x})$  is the unit eigenvector of the estimated Riemannian matrix  $\mathcal{H}\hat{f}(\mathbf{x})$  within the tangent space  $T_{\mathbf{x}}$  associated with the smallest eigenvalue  $\hat{\lambda}_2(\mathbf{x})$ ; see Appendix B1 for the expression for  $\mathcal{H}\hat{f}(\mathbf{x})$ . While the standard SCMS algorithm is incapable of identifying the (directional) density function and its ridge on  $\mathbb{S}^2$  (recall Figure 1), we propose our directional SCMS (DirSCMS) algorithm with an iterative formula as:

$$\tilde{\mathbf{x}}^{(t+1)} \leftarrow \mathbf{x}^{(t)} - \hat{\mathbf{v}}_2(\mathbf{x}^{(t)}) \hat{\mathbf{v}}_2(\mathbf{x}^{(t)})^T \left[ \frac{\sum_{i=1}^n \mathbf{X}_i L' \left( \frac{1 - \mathbf{X}_i^T \mathbf{x}^{(t)}}{b^2} \right)}{\left\| \sum_{i=1}^n \mathbf{X}_i L' \left( \frac{1 - \mathbf{X}_i^T \mathbf{x}^{(t)}}{b^2} \right) \right\|_2} \right], \quad (7)$$

and  $\mathbf{x}^{(t+1)} \leftarrow \frac{\tilde{\mathbf{x}}^{(t+1)}}{\|\tilde{\mathbf{x}}^{(t+1)}\|_2}$  for  $t = 0, 1, \dots$ , recalling that  $\{\mathbf{X}_1, \dots, \mathbf{X}_n\}$  consists of Cartesian coordinates of the observations on  $\mathbb{S}^2$ . At a

high level, our DirSCMS algorithm updates a given point  $\mathbf{x}^{(t)}$  on  $\mathbb{S}^2$  along the direction of the (estimated) projected Riemannian gradient  $\hat{\mathbf{v}}_2(\mathbf{x}^{(t)}) \hat{\mathbf{v}}_2(\mathbf{x}^{(t)})^T \text{grad } \hat{f}(\mathbf{x}^{(t)})$ . It leads to an iterative sequence  $\{\mathbf{x}^{(t)}\}_{t=0}^\infty \subset \mathbb{S}^2$  that converges to the estimated density ridge (or our practical filament model)  $R(\hat{f})$ ; see Figure 2 for graphical illustrations. More results about the convergence of our DirSCMS algorithm can be found in Section 4.2 in Zhang & Chen (2021b). In Appendix B2, we describe a more general formulation of the DirSCMS algorithm on  $\mathbb{S}^2$  that takes into account the stellar properties of the observational data in its iteration. Additionally, we discuss how to quantify the uncertainty levels of filamentary points on the estimated density ridge  $R(\hat{f})$  with our DirSCMS algorithm and bootstrap techniques in Appendix C. Given that different bootstrap schemes give rise to linearly correlated uncertainty measures for the estimated filaments (see Appendix C4), we will implement the nonparametric bootstrap with the number of bootstrapping times as  $B = 100$  for measuring the uncertainty of any estimated filament in this paper.

## 2.3 SCMS Algorithm on the Light Cone $\mathbb{S}^2 \times \mathbb{R}$

In the previous subsection, we have offered our first extended SCMS algorithm to detect cosmic filaments under the 2D spherical geometry. Although this extension is convenient for the local analysis of 2D spherical cosmic web structures within some thin redshift slices, it will inevitably miss some light-of-sight filaments in the large-scale structure of our universe. Therefore, we provide the second extension of the SCMS algorithm to handle the filament finding task in the 3D light cone  $\mathbb{S}^2 \times \mathbb{R}$ .

### 2.3.1 Filament Model on $\mathbb{S}^2 \times \mathbb{R}$

Suppose that the data comprise  $n$  observations  $(\mathbf{X}_1, Z_1), \dots, (\mathbf{X}_n, Z_n)$  sampled from a (directional-linear) density function  $f_{dl}(\mathbf{x}, z)$  in the 3D light cone (or equivalently, the 3D redshift space)  $\mathbb{S}^2 \times \mathbb{R}$ , where  $\{\mathbf{X}_i\}_{i=1}^n$  encodes their Cartesian coordinates on the (unit) celestial sphere  $\mathbb{S}^2$  and  $\{Z_i\}_{i=1}^n$  are their redshift values. The traditional avenue to detect cosmic filaments in the 3D redshift space is to convert the redshifts into comoving distances so that each observation has its unique representation in the Euclidean space  $\mathbb{R}^3$  (Tempel et al. 2014). However, this conversion relies on a specific cosmological model and needs to handle the finger-of-god effects or other redshift distortions in designing the conversion formula. Due to these two factors, the resulting cosmic web structures tend not to be very flexible in downstream analyses.

As a result, we consider estimating the matter/galaxy density function  $f_{dl}(\mathbf{x}, z)$  and its filamentary structures directly from the data  $\{(X_i, Z_i)\}_{i=1}^n$  on the 3D light cone  $\mathbb{S}^2 \times \mathbb{R}$ . In particular, the density function is estimated by the directional-linear KDE (García-Portugués et al. 2013, 2015) as:

$$\widehat{f}_{dl}(\mathbf{x}, z) = \frac{C_L(b_1)}{nb_2} \sum_{i=1}^n L\left(\frac{1-\mathbf{x}^T X_i}{b_1^2}\right) K\left(\left\|\frac{z-Z_i}{b_2}\right\|_2^2\right), \quad (8)$$

where  $L(\cdot)$  and  $K(\cdot)$  are the directional and linear kernel functions while  $b_1$  and  $b_2$  are the smoothing bandwidth parameters for directional and linear data components. In our practical applications, we take  $L(r) = e^{-r}$  as the directional (von Mises) kernel and  $K(r) = \frac{1}{\sqrt{2\pi}} e^{-\frac{r}{2}}$  as the linear (Gaussian) kernel.

As before, the directional-linear KDE (8) provides a plug-in estimator  $R(\widehat{f}_{dl})$  of the density ridge (or the theoretical filament model) of the underlying density function  $f_{dl}$  defined as:

$$R(f_{dl}) = \left\{ (\mathbf{x}, z) \in \mathbb{S}^2 \times \mathbb{R} : V_{dl}(\mathbf{x}, z)^T \text{grad } f_{dl}(\mathbf{x}, z) = \mathbf{0}, \right. \\ \left. \lambda_{dl,2}(\mathbf{x}, z) < 0 \right\}, \quad (9)$$

where  $V_{dl}(\mathbf{x}, z) = [\mathbf{v}_{dl,2}(\mathbf{x}, z), \mathbf{v}_{dl,3}(\mathbf{x}, z)] \in \mathbb{R}^{4 \times 2}$  has its columns as the orthonormal eigenvectors inside the tangent space  $T_{(\mathbf{x}, z)}$  of  $\mathbb{S}^2 \times \mathbb{R}$  associated with the last two eigenvalues  $\lambda_{dl,2}(\mathbf{x}, z) \geq \lambda_{dl,3}(\mathbf{x}, z)$  of the Riemannian Hessian  $\mathcal{H}f_{dl}(\mathbf{x}, z) \in \mathbb{R}^{4 \times 4}$ ; see Appendix A for the expressions of  $\text{grad } f_{dl}(\mathbf{x}, z)$  and  $\mathcal{H}f_{dl}(\mathbf{x}, z)$ .

### 3.2.2 Filament Estimation on $\mathbb{S}^2 \times \mathbb{R}$ : Directional-Linear SCMS Algorithm

While the generalization of KDE and density ridges (or our cosmic filament model) from the density function  $f$  on the celestial sphere  $\mathbb{S}^2$  to  $f_{dl}$  on the 3D light cone  $\mathbb{S}^2 \times \mathbb{R}$  is not very challenging, the extension of the SCMS algorithm to the directional-linear data  $\{(X_i, Z_i)\}_{i=1}^n$  requires special attention. A naive generalization from the mean shift algorithm to its SCMS counterpart as how the standard SCMS method does (Ozertem & Erdogmus 2011) will lead to an incorrect estimate of  $R(\widehat{f}_{dl})$ ; see the related discussion in Section 4 of Zhang & Chen (2021c). Here, we formulate the correct SCMS iteration formula at point  $(\mathbf{x}^{(t)}, z^{(t)}) \in \mathbb{S}^2 \times \mathbb{R}$  as:

$$\begin{pmatrix} \tilde{\mathbf{x}}^{(t+1)} \\ z^{(t+1)} \end{pmatrix} \leftarrow \begin{pmatrix} \mathbf{x}^{(t)} \\ z^{(t)} \end{pmatrix} \\ + \eta \cdot \widehat{V}_{dl}(\mathbf{x}^{(t)}, z^{(t)}) \widehat{V}_{dl}(\mathbf{x}^{(t)}, z^{(t)})^T \mathbf{H} \cdot \Xi(\mathbf{x}^{(t)}, z^{(t)}), \quad (10)$$

and  $\mathbf{x}^{(t+1)} \leftarrow \frac{\tilde{\mathbf{x}}^{(t+1)}}{\|\tilde{\mathbf{x}}^{(t+1)}\|_2}$  for  $t = 0, 1, \dots$ , where  $\widehat{V}_{dl}(\mathbf{x}, z) = [\widehat{\mathbf{v}}_{dl,2}(\mathbf{x}, z), \widehat{\mathbf{v}}_{dl,3}(\mathbf{x}, z)]$  has its columns as the last two eigenvectors of the estimated Riemannian Hessian  $\mathcal{H}\widehat{f}_{dl}(\mathbf{x}, z)$  within the tangent space  $T_{(\mathbf{x}, z)}$  of  $\mathbb{S}^2 \times \mathbb{R}$ ,  $\mathbf{H} = \text{Diag}\left(\frac{1}{b_1^2}, \dots, \frac{1}{b_1^2}, \frac{1}{b_2^2}\right) \in \mathbb{R}^{4 \times 4}$  is a diagonal (bandwidth) matrix, and

$$\Xi(\mathbf{x}^{(t)}, z^{(t)}) = \begin{pmatrix} \frac{\sum_{i=1}^n X_i \cdot L\left(\frac{1-\mathbf{x}^{(t)T} X_i}{b_1^2}\right) K\left(\left\|\frac{z^{(t)}-Z_i}{b_2}\right\|_2^2\right)}{\sum_{i=1}^n L\left(\frac{1-\mathbf{x}^{(t)T} X_i}{b_1^2}\right) K\left(\left\|\frac{z^{(t)}-Z_i}{b_2}\right\|_2^2\right)} - \mathbf{x}^{(t)} \\ \frac{\sum_{i=1}^n Z_i \cdot L\left(\frac{1-\mathbf{x}^{(t)T} X_i}{b_1^2}\right) K'\left(\left\|\frac{z^{(t)}-Z_i}{b_2}\right\|_2^2\right)}{\sum_{i=1}^n L\left(\frac{1-\mathbf{x}^{(t)T} X_i}{b_1^2}\right) K\left(\left\|\frac{z^{(t)}-Z_i}{b_2}\right\|_2^2\right)} - z^{(t)} \end{pmatrix}, \quad (11)$$

is the (directional-linear) mean shift vector at the iterative point  $(\mathbf{x}^{(t)}, z^{(t)}) \in \mathbb{S}^2 \times \mathbb{R}$  at step  $t$ ; see Appendix B3 for more details. We name (10) as the DirLinSCMS algorithm.

There are two major differences of the DirLinSCMS iteration in the 3D light cone  $\mathbb{S}^2 \times \mathbb{R}$  to the standard SCMS algorithm in Section 2.1 and our preceding DirSCMS algorithm in Section 2.2. First, we scale the mean shift vector  $\Xi(\mathbf{x}^{(t)}, z^{(t)})$  by a diagonal (bandwidth) matrix  $\mathbf{H}$  in (10) to ensure that the DirLinSCMS iteration follows the correct projected gradient direction of  $\widehat{f}_{dl}(\mathbf{x}^{(t)}, z^{(t)})$  at step  $t$ . Second, even under the smooth von Mises and Gaussian kernels, the DirLinSCMS iteration (10) still requires a step size parameter to control its convergence. As the step size parameter is notoriously difficult to tune in any application of gradient ascent methods, we provide a theoretically motivated and practically effective guideline to choose the step size parameter  $\eta$  in (10) as:

$$\eta = \min\{b_1 b_2, 1\}, \quad (12)$$

where the upper bound 1 is set to prevent  $\eta$  from being too large when the smoothing bandwidth parameters are chosen to be large. In Section 3.3, we apply our DirLinSCMS algorithm to the friends-of-friends (FoF) halos of the Illustris simulation and study the stability of detected filamentary structures under the effects of peculiar velocities. Analogous to our DirSCMS algorithm on  $\mathbb{S}^2$ , one can also resort to the bootstrap technique (Appendix C) to quantify the uncertainties of the estimated density ridge  $R(\widehat{f}_{dl})$  on  $\mathbb{S}^2 \times \mathbb{R}$  detected by our DirLinSCMS algorithm.

### 2.4 Cosmic Nodes on the Filaments

We have discussed so far our methodology to detect cosmic filaments from discrete observations on the celestial sphere  $\mathbb{S}^2$  and the 3D light cone  $\mathbb{S}^2 \times \mathbb{R}$ . These one-dimensional structures occupy roughly half of the mass in our universe (Cautun et al. 2014; Cui et al. 2018). Further, as cosmic time evolves, galaxies within the filaments and in the field gradually fall into galaxy clusters (Navarro et al. 1995; Springel et al. 2005; Kuchner et al. 2022), creating the most compact structures that are gravitationally bound in the cosmic web. Here, we describe two potentially overlapping types of cosmic nodes on our density ridge model that are strong candidates for galaxy clusters in an astrophysical sense (Malavasi et al. 2022).

- **Local modes.** One type of regions where galaxy clusters are commonly found are in the local modes (called local peaks or maxima) of the matter/galaxy density function, which signal the locations where galaxies/particles are highly concentrated. They are subsumed in our cosmic filament model based on the density ridge (c.f., Equations (1), (4), and (9)), manifesting the property that cosmic filaments bridge the connection between galaxy clusters. We identify the set of local modes on filaments via the mean shift algorithm, which is the prototype of the above SCMS algorithm; see Appendix B4 for details.

- **Knots.** Besides local modes, another type of indicators on filaments for galaxy clusters are the intersection points of two or more pieces of the filaments (Aragón-Calvo et al. 2010a), which we call knots. To identify the knots on a given filamentary structure, we implement the metric graph reconstruction algorithm (Aanjaneya et al. 2011; Lecci et al. 2014); see Appendix B4 for details.

## 3 APPLICATIONS

This section describes the application of our extended SCMS algorithms on  $\mathbb{S}^2$  and  $\mathbb{S}^2 \times \mathbb{R}$  to the survey and simulation data. We

first revisit our toy example of a cross-shaped filament at the North pole in Section 2.1 and further compare our proposed DirSCMS algorithm with other SCMS typed filament finders as well as the well-known DisPerSE algorithm in Section 3.1. Then, we utilize the DirSCMS algorithm to detect cosmic filaments and nodes on some thin slices of the SDSS-IV galactic data in Section 3.2 and leverage the DirLinSCMS algorithm to identify filamentary structures from dark matter halos of the Illustris simulation in Section 3.3.

### 3.1 Toy example: Cross-Shaped Filament At the North Pole

We show in Section 2.1 that our proposed DirSCMS algorithm outperforms the standard SCMS method in recovering the true filament structure (*i.e.*, a cross-shaped filament on  $\mathbb{S}^2$  with its center at the North pole) given a mock dataset with 2000 noisy observations. Here, we further compare our DirSCMS algorithm with other SCMS typed filament finders, including the Density Ridge Estimation Describing Geospatial Evidence (DREDGE; Moews et al. 2021a; Moews et al. 2021b) and SCMS algorithm with HEALPix (Carrón Duque et al. 2022). Additionally, we compare our method with the widely used Discrete Persistent Structure Extractor (DisPerSE; Sousbie 2011; Sousbie et al. 2011).

#### 3.1.1 Method Description

As mentioned in Section 2.2, DREDGE<sup>5</sup> leverages the haversine formula to calculate the geodesic distance between a pair of points and estimate the matter/galaxy density function on  $\mathbb{S}^2$ . It also inherits the main scheme of the standard SCMS algorithm in its ridge estimation; see Moews et al. (2021b). In our application of DREDGE to the mock dataset under the angular (RA,DEC) coordinate, the smoothing bandwidth parameter is chosen as the average geodesic distance from every observation to its 20 nearest neighbors on  $\mathbb{S}^2$ .

The SCMS algorithm introduced in Carrón Duque et al. (2022), on the other hand, utilizes the HEALPix at resolution  $N_{side} = 1024$  to compute the estimated galaxy density, its gradient, and Hessian on  $\mathbb{S}^2$ , whose kernel function is the Gaussian kernel evaluated on the geodesic distance. The choice of the bandwidth parameter does not have a large influence on the SCMS algorithm with HEALPix in this toy example, and we select it to be optional among a reasonable range of candidate values.

The filament detection with DisPerSE consists of three main steps. First, DisPerSE makes use of the Delaunay tessellation to construct the simplicial complex from a set of discrete observations and assigns the density to each simplex according to the inverse volume of its dual Voronoi cell (van de Weygaert & Schaap 2009; Boots et al. 2009). Then, the discrete gradients, critical simplices, as well as the discrete Morse-Smale complex are derived on top of the discrete density function (Scoville 2019). Notice that the filaments by DisPerSE are defined as the gradient flows that directly connect the maxima with saddle points. Second, DisPerSE follows the concept of topological persistence (Edelsbrunner et al. 2000) to purify the discrete Morse-Smale complex. Specifically, it assigns a density ratio to each pair of connected critical simplices and removes those pairs whose ratios are less than some persistence ratio threshold with respect to a random discrete Poisson distribution from the discrete Morse-Smale complex. In the DisPerSE software<sup>6</sup>, the persistence ratio threshold

<sup>5</sup> The DREDGE code is on <https://pypi.org/project/dredge>.

<sup>6</sup> See <http://www2.iap.fr/users/sousbie/web/html/index41d.html>.

**Table 1.** Hausdorff distance [deg] between the estimated filament  $\widehat{R}$  by each filament finding method and the true cross-shaped filament  $R$ .

Standard SCMS	DirSCMS	DREDGE	SCMS with HEALPix	2D Angular DisPerSE	3D Cartesian DisPerSE
13.079	<b>3.486</b>	5.408	4.997	5.907	5.754

is specified in units of “ $\sigma$ ” based on the significance level and serves as an important parameter of DisPerSE that controls the smoothness of the initial filamentary structures. Finally, DisPerSE smooths the yielded filaments by iteratively averaging their spatial positions.

Given the versatility of DisPerSE, we apply it to both the 2D angular (RA,DEC) and 3D Cartesian coordinates of the observations in the mock dataset. The persistence ratio threshold for each DisPerSE application is chosen to be optimal among several candidate values, and the final output filaments are smoothed five times.

#### 3.1.2 Results

With the mock dataset around the cross-shaped filament at the North pole on  $\mathbb{S}^2$  as the inputs, we present the filaments estimated by DREDGE, SCMS algorithm with HEALPix, and DisPerSE in Figure 3. For better comparison, one can recall the filaments detected by the standard SCMS and our proposed DirSCMS algorithm in Figure 1. All the estimated filaments are post-cleaned by trimming those filamentary points outside the sky footprint of the input observations.

As demonstrated by the top row of Figure 3, DREDGE fails to converge to the true cross-shaped filament near the North pole on  $\mathbb{S}^2$ . The SCMS algorithm with HEALPix, on the other hand, precisely approximates the true cross-shaped filament in the regions with relatively low declination but fails to recover the filament with declination greater than  $80^\circ$ . This inferior performance around the North pole may be due to its usage of the angular coordinate system, which is not completely isotropic on  $\mathbb{S}^2$ , and the numerical instabilities in computing the derivatives of the estimated density with the HEALPix scheme on  $\mathbb{S}^2$ . As for the bottom row of Figure 3, DisPerSE produces some estimated filaments that recover parts of the true filamentary structure. However, the filaments by DisPerSE are irregular and contain many spurious components compared with the filament yielded by our DirSCMS algorithm.

To conclude this artificial cross-shaped filament example, we compute the distance error distribution  $\{d_g(\mathbf{x}, R) \text{ for all } \mathbf{x} \in \widehat{R}\}$  from each estimated filament  $\widehat{R}$  yielded by the standard SCMS, DREDGE, SCMS with HEALPix, DisPerSE, and our DirSCMS algorithms to the true cross-shaped filament  $R$ , where  $d_g(\mathbf{x}, R) = \min \{d_g(\mathbf{x}, \mathbf{y}) : \mathbf{y} \in R\}$  with  $d_g(\cdot, \cdot)$  defined in (C2). This metric reveals how close the filamentary points in  $\widehat{R}$  to the true structure  $R$ ; see the top right panel of Figure 3. On the other hand, we also calculate the distance error distribution  $\{d_g(\mathbf{y}, \widehat{R}) \text{ for all } \mathbf{y} \in R\}$  from the true cross-shaped filament  $R$  to each estimated filament  $\widehat{R}$ , which measures how well  $\widehat{R}$  approximates the entire true structure  $R$ ; see the bottom right panel of Figure 3. Our proposed DirSCMS algorithm exhibits relatively low distance errors in terms of the above two metrics, which can be further demonstrated by the Hausdorff distance

$$d_H(R, \widehat{R}) = \max \left\{ \sup_{\mathbf{x} \in \widehat{R}} d_g(\mathbf{x}, R), \sup_{\mathbf{y} \in R} d_g(\mathbf{y}, \widehat{R}) \right\}$$

in Table 1. Thus, our DirSCMS algorithm outperforms all the competitors in recovering the true filament under the spherical geometry.

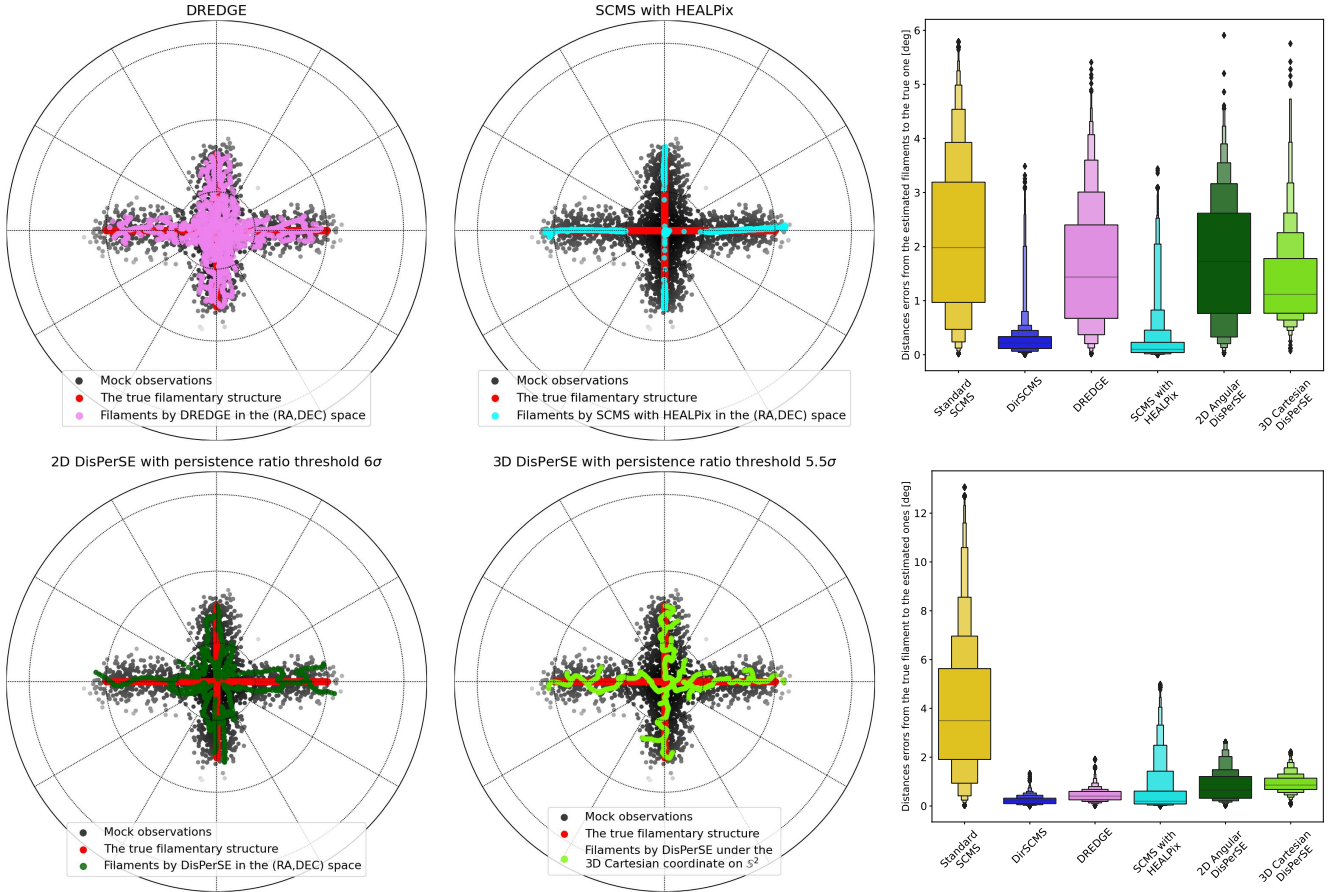


**Figure 3.** Comparisons of different filament finding algorithms applied to the mock dataset. *Top Left and Top Middle:* The estimated filaments yielded by DREDGE and SCMS with HEALPix together with the true cross-shaped filament and the mock observations around it. *Bottom Left and Bottom Middle:* the estimated filaments by DisPerSE under the 2D angular and 3D Cartesian coordinates on  $\mathbb{S}^2$ , respectively. *Top Right:* The distance error distribution from the estimated filament by each filament finding method to the true cross-shaped filament. *Bottom Right:* The distance error distribution from the true cross-shaped filament to the estimated one by each filament finding method. We present these distance error distributions in terms of the letter-value plots (Hofmann et al. 2017).

### 3.2 Sloan Digital Sky Survey

We now apply our method to the galaxy sample from Data Release 16 of the Sloan Digital Sky Survey, Fourth Phase (SDSS-IV; Ahumada et al. 2020). We aim at comparing our proposed DirSCMS algorithm with the standard SCMS and DisPerSE methods in recovering the cosmic filaments in the region of high declination. Given that the SDSS-IV galaxies mainly come from regions of relatively low declination, we create a mock galactic data sample by rotating the galaxies on the celestial sphere  $\mathbb{S}^2$ .

#### 3.2.1 Data Description

The SDSS-IV consists of three main surveys in this release: the Extended Baryon Oscillation Spectroscopic Survey (eBOSS; Dawson et al. 2016), Mapping Nearby Galaxies at APO (MaNGA; Bundy et al. 2015), and the APO Galactic Evolution Experiment 2 (APOGEE-2; Majewski et al. 2017), which together covers around 35.28% of the sky ( $14,555 \text{ deg}^2$ ). In particular, eBOSS extends the galaxy measurement of its predecessor BOSS, the eBOSS, from the redshift range  $z < 0.6$  to  $z < 1$ . Moreover, compared with the previous SDSS data release, eBOSS provides 860,935 new optical spectra of galaxies and quasars in this release and reprocesses its spectra using the latest version of the data reduction pipelines (Bolton et al. 2012; Dawson

et al. 2013). Our following analysis relies primarily on all the spectra classified as galaxies by SDSS-IV. Among them, we focus on those galaxies with definite positive redshift values.

As revealed by Figure 3, the standard SCMS and DisPerSE algorithms can produce some highly biased filaments under the (RA,DEC) coordinate system of the survey data, especially in the regions of high declination. While the SDSS-IV generally observes astronomical objects in the regions of relatively low declination, some future wide sky surveys, such as EUCLID (Cagliari et al. 2021) and LSST (Bianco et al. 2022), are planning to observe the sky footprints with higher declination values. Therefore, we intend to study how the standard SCMS, DisPerSE, and our proposed DirSCMS algorithms behave if our observational data lie mainly on the region of high declination. To this end, we consider two thin slices  $0.05 \leq z < 0.055$  at low redshift and  $0.46 \leq z < 0.465$  at high redshift and extract the above SDSS-IV galaxies within these two redshift slices that locate in the North Galactic Cap ( $100^\circ < \text{RA} < 270^\circ$ ,  $-5^\circ < \text{DEC} < 70^\circ$ ). The total number of resulting galaxies within the selected celestial region is 22,709 for the low redshift slice  $0.05 \leq z < 0.055$  and 14,486 for the high redshift slice  $0.46 \leq z < 0.465$ . Then, we compute the spherical mean  $\frac{\sum_{i=1}^n \mathbf{X}_i}{\|\sum_{i=1}^n \mathbf{X}_i\|_2}$  of the galaxies based on their Cartesian coordinates  $\mathbf{X}_1, \dots, \mathbf{X}_n \in \mathbb{S}^2$  in each redshift slice and rotate the galaxies within each redshift slice such that their new spherical

mean is  $\mu_0 = (0, 0, 1) \in \mathbb{S}^2$ . Such a rotation can be easily done by multiplying the rotation matrix (C7) to the Cartesian coordinate of each galaxy. Hence, we obtain two mock galaxy samples for the low and high redshift slices on  $\mathbb{S}^2$  whose center is at the North pole.

### 3.2.2 Results

We first apply the standard SCMS, DisPerSE, and our proposed DirSCMS algorithms to the mock galaxy sample in the low redshift slice  $0.05 \leq z < 0.055$  in order to detect the cosmic filaments (as well as the associated cosmic nodes). The bandwidth parameter for the standard SCMS algorithm is taken according to Equation (A1) in Appendix A of Chen et al. (2015b) as:

$$b_{\text{Euc}} = A_0 \left( \frac{1}{d+2} \right)^{\frac{1}{d+4}} n^{-\frac{1}{d+4}} \sigma_{\text{min}} \quad (13)$$

with dimension  $d = 2$  and scale factor  $A_0 = 0.6$  in this case, where  $\sigma_{\text{min}}$  is minimal standard deviation across all the coordinates; see also Proposition 1 in Chacón et al. (2011). During the application of DisPerSE, we use both the 2D angular (RA,DEC) coordinates and 3D (RA,DEC, $z$ ) coordinates of the mock galaxies as inputs and set the persistence threshold ratio as  $3\sigma$ . In addition, when utilizing DisPerSE to detect cosmic filaments under the 3D (RA,DEC, $z$ ) space, we transform the coordinates of input galaxies to their Cartesian counterparts via the WMAP-9 cosmology. The output filaments by DisPerSE are iteratively smoothed for 5 times. As for the bandwidth parameter for our DirSCMS algorithm, we slightly modify the rule of thumb on  $\mathbb{S}^2$  in Proposition 2 of García-Portugués (2013) as:

$$b_{\text{Dir}} = B_0 \left[ \frac{8 \sinh^2(\widehat{\kappa})}{\widehat{\kappa} [(1 + 4\widehat{\kappa}^2) \sinh(2\widehat{\kappa}) - 2\widehat{\kappa} \cosh(2\widehat{\kappa})] n} \right]^{\frac{1}{6}} \quad (14)$$

with  $\widehat{\kappa} = \frac{\bar{R}(3-\bar{R})}{1-\bar{R}^2}$ , where  $\bar{R} = \frac{\|\mathbf{X}_i\|_2}{n}$  given the Cartesian coordinates of galaxies  $\mathbf{X}_1, \dots, \mathbf{X}_n$  on  $\mathbb{S}^2$  and we take  $B_0 = 0.25$  to avoid the over-smoothing effect (Sheather 2004). Finally, to reduce the production of spurious filaments, we remove 20% of galaxies with low estimated density values before the iterations of the standard SCMS and our DirSCMS algorithms; see Step 2 of Algorithm 1 in Appendix B1.

As shown by Figure 4, the standard SCMS algorithm misses a lot of potential filamentary structures within the regions with  $\text{DEC} > 65^\circ$ . DisPerSE under both the 2D angular (RA,DEC) and 3D (RA,DEC, $z$ ) coordinates, though capturing parts of sensible filaments within the high-declination regions, produces many spurious filamentary structures. Moreover, the filamentary points detected by the standard SCMS and DisPerSE algorithms have considerably high uncertainties, especially when the filamentary points lie in the region of high declination. On the contrary, our proposed DirSCMS algorithm is able to recover the filaments with high confidence whatever declination the galaxies are located at. To further demonstrate the isotropy and adaptivity of our DirSCMS algorithm on  $\mathbb{S}^2$ , we quantitatively analyze how the filamentary structures recovered by the above filament finding algorithms would change when the declination values of the galaxies vary. To this end, we estimate the two sets of filaments with each filament finding algorithm based on the mock galaxy sample before rotation (*i.e.*, in the original SDSS observational region of low declination) and after rotation (*i.e.*, in the region of high declination and centering at the North pole), respectively. Then, we compute the distance error from each point of the filamentary set in the high-declination region to the one in the original low-declination region on  $\mathbb{S}^2$ , conditioning that the spherical means of these two sets of filaments are the same. The distance metric is based on the

geodesic distance on  $\mathbb{S}^2$ ; see (C2). These distance error distributions are depicted in the bottom middle panel of Figure 4. The filamentary structures in low and high-declination regions by the standard SCMS and DisPerSE algorithms exhibit large discrepancies in terms of their distance error distributions, suggesting that these filament finding algorithm is highly unstable with respect to any change of the declination values of the input galaxies on  $\mathbb{S}^2$ . In stark contrast to them, the filaments estimated by our DirSCMS algorithm in low and high-declination regions are identical (*i.e.*, having zero distance errors for all the filamentary points) whenever the bandwidth parameter is held constant, proving that our DirSCMS algorithm is invariant to any data rotation on  $\mathbb{S}^2$  and thus adaptive to the spherical geometry. The results for the mock galaxy sample in the high redshift slice  $0.46 \leq z < 0.465$  are similar and shown in Figure 5.

### 3.3 Illustris Simulation

Our second astronomical application targets at demonstrating the effectiveness and stability of our DirLinSCMS algorithm (Section 2.3) when it is applied to astronomical data in the 3D (RA,DEC, $z$ ) space. The analysis is performed on the friends-of-friends (FoF) halo of the Illustris simulation project (Vogelsberger et al. 2014a; Genel et al. 2014; Vogelsberger et al. 2014b; Sijacki et al. 2015).

#### 3.3.1 Data Description

The Illustris presents a collection of cosmological hydrodynamical simulations with delicate physical models targeting at the formation and evolution of galaxies across cosmic time (Nelson et al. 2015). Each snapshot of the Illustris simulation is self-consistently conducted in a 3D cube with side length  $75h^{-1}$  Mpc  $\approx 106.5$  Mpc under the WMAP-9 cosmology and evolves from redshift  $z = 127$  to the present day  $z = 0$ . Within these periodic simulation boxes, there are five types of resolution elements, consisting of dark matter particles, gas cells, gas tracers, stellar and stellar wind particles, as well as black hole sinks. The final public data release of the Illustris simulation includes six primary realizations with different resolution levels or physics implementations of the Illustris volume, each of which has 136 snapshots at different available redshifts from  $z = 46.77$  to  $z = 0$ . Every snapshot also contains a group catalog with FoF halos and SUBFIND (Springel et al. 2001; Onions et al. 2012) subhalos.

Given that dark matter halos incubate galaxies and serve as fundamental nonlinear units of cosmic structures (Frenk & White 2012; Wechsler & Tinker 2018), our following filament detection tasks are based on the FoF halos in the snapshot at redshift  $z = 0$  from the Illustris-3 simulation<sup>7</sup>. The standard FoF algorithm (Turner & Gott 1976; Zeldovich et al. 1982) with linking length 0.2 is performed on the dark matter particles so as to identify 131,727 halos within the associated simulation box at redshift  $z = 0$ .

To study the stability of our proposed DirLinSCMS algorithm in detecting filamentary structures from Illustris halos against the redshift distortions due to the effects of peculiar velocities, we mimic the data coordinates that are commonly encounter in astronomical surveys. Specifically, we convert the 3D coordinates of the above Illustris halo data in the periodic box to their (RA,DEC, $z$ ) coordinates by assuming an observer placed at (0,0,0). This can be achieved, for instance, by modifying the “ra\_dec\_z” function in the “mock\_observables” module of Halotools (v0.7); see Hearin et al.

<sup>7</sup> The data can be downloaded at <https://www.illustris-project.org/data/downloads/Illustris-3/>.

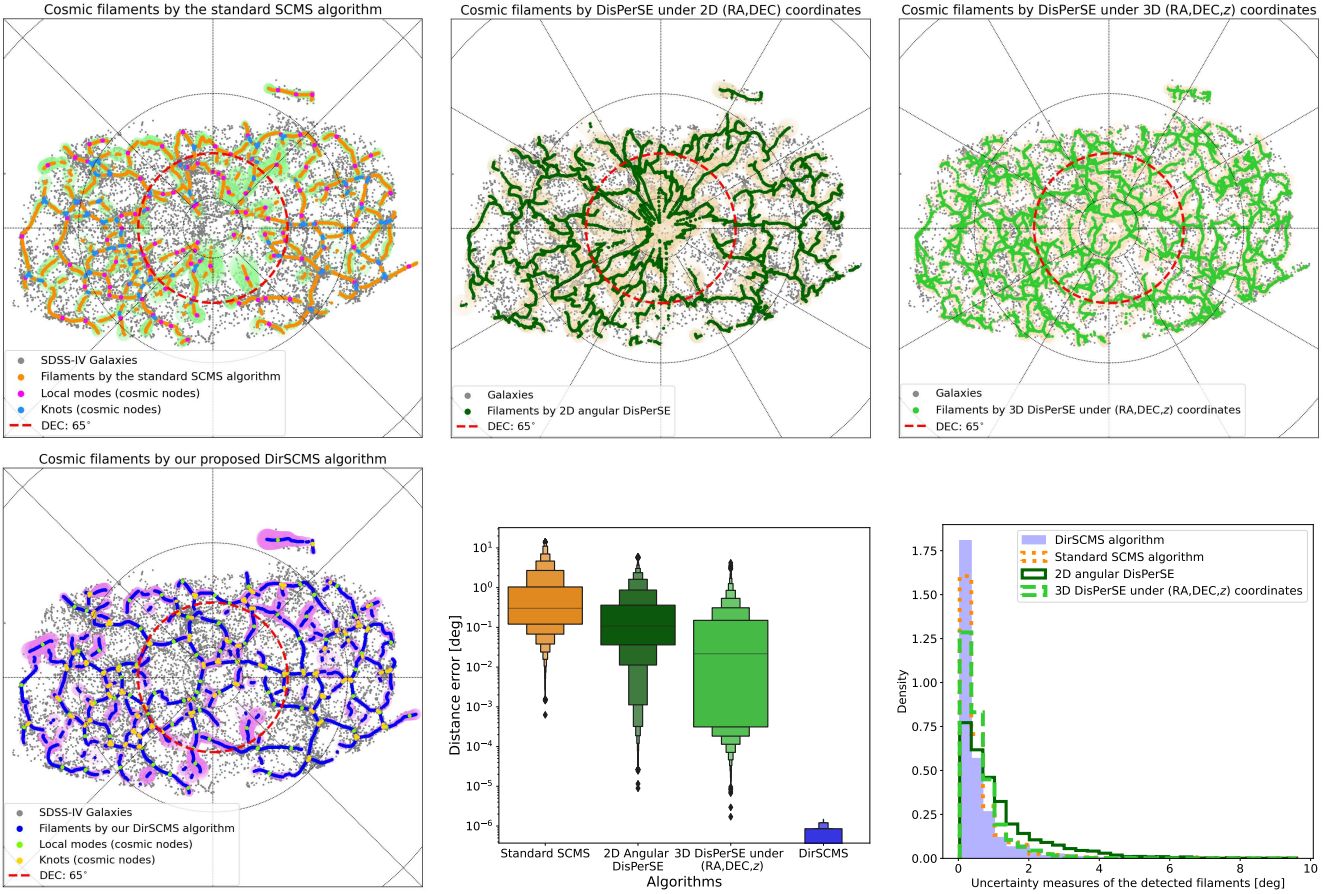


**Figure 4.** Comparisons of cosmic filaments detected by the standard SCMS, DisPerSE, and our proposed DirSCMS algorithms on the mock galaxy sample in the low redshift slice  $0.05 \leq z < 0.055$ . *Top Row and Bottom Left:* the cosmic filaments (and associated cosmic nodes) recovered by the standard SCMS, DisPerSE under the 2D angular (RA, DEC) and 3D (RA, DEC,  $z$ ) coordinate systems, and our DirSCMS algorithms, respectively, where the light colored areas around the filaments indicate the magnitude of uncertainty measure for each filamentary point. In the *Upper Right* panel, we project the filaments in the 3D (RA, DEC,  $z$ ) space onto the 2D angular (RA, DEC) space for visualization. *Bottom Middle:* The letter-value plots of distance errors from the filaments in the high-declination region to the ones in the original low-declination region on  $\mathbb{S}^2$  estimated by the standard SCMS, DisPerSE, and our DirSCMS algorithms. *Bottom Right:* The histograms of uncertainty measures for the filaments recovered by all these algorithms.

(2017) for details. After the change of coordinates, each halo has two different redshift values, one in the observed redshift space (with the effects of peculiar velocities) and the other in the true/cosmological redshift space (without the effects of peculiar velocities). These two redshift values, together with the (RA, DEC) coordinate, encodes two distinct positions in the 3D light cone  $\mathbb{S}^2 \times \mathbb{R}$  for each halo.

### 3.3.2 Results

We apply our DirLinSCMS algorithm to the (RA, DEC,  $z$ ) coordinates of the halo data under the observed and cosmological redshifts respectively, yielding two set of filamentary structures; see the left panel of Figure 6. The bandwidth parameters  $b_1, b_2$  for the directional and linear data parts are chosen via (14) and (13) with scale factors  $B_0 = 0.5$  and  $A_0 = 40$  in the observed redshift space. When detecting the filaments in the true/cosmological redshift space, we apply the same set of bandwidth parameters as the one in the observed redshift space. It is worth mentioning that the resulting filamentary structures from our DirLinSCMS algorithm are sensitive to the choices of its bandwidth parameters and a useful guideline to select  $b_1, b_2$  is to ensure that their values are balanced and of roughly the same scale under the input data. The stability of our DirLinSCMS algo-

rithm against the redshift distortions, however, is relatively robust to different choices of the bandwidth parameters. More discussions about the bandwidth selection for our DirLinSCMS algorithm and its stability results can be found in Appendix B3. For comparison, we also implement the standard SCMS and DisPerSE algorithms on the Cartesian coordinates of the halo data under the WMAP-9 cosmology in both the observed and cosmological redshift spaces. The bandwidth parameter of the standard SCMS algorithm is selected as (13) with  $A_0 = 1.5$  and  $d = 3$ . The persistence ratio threshold is set to be  $9\sigma$  during the application of DisPerSE, and the output filaments are smoothed 5 times. All the final filamentary structures produced by each algorithm are presented under their 3D coordinates inside the  $(75 \text{ Mpc}/h)^3$  simulation box; see the top row of Figure 6.

It is noticeable from the 3D visualizations of filaments in Figure 6 that the two sets of filaments in the observed and cosmological redshift shapes are more aligned and consistent with each other under our DirLinSCMS algorithm than the standard SCMS and DisPerSE method. We compute the distance errors from the filaments in the observed redshift space to the ones in the cosmological redshift space based on these three filament finding algorithms respectively, and plot their distributions in terms of the comparative letter-value plots and histograms at the bottom row of Figure 6. Both the two-sample

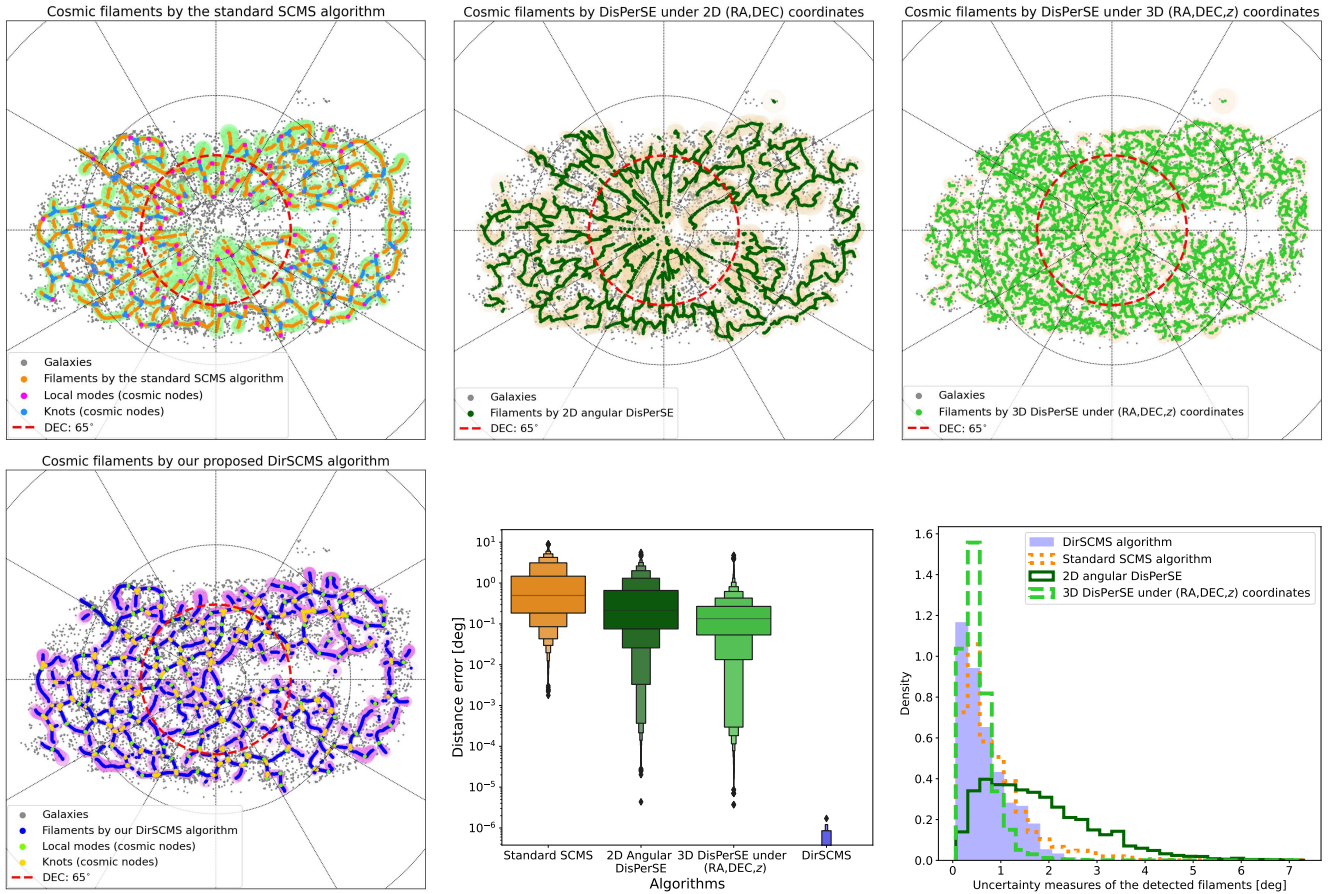


**Figure 5.** Comparisons of cosmic filaments detected by the standard SCMS, DisPerSE, and our proposed DirSCMS algorithms on the mock galaxy sample in the high redshift slice  $0.46 \leq z < 0.465$ . The detailed description for each panel can be found in Figure 4.

Welch’s t-test and Kolmogorov-Smirnov test between the distance errors by our DirLinSCMS algorithm against the other two methods yield essentially zero p-values. It validates the visual finding that our DirLinSCMS algorithm is more robust to the redshift distortions introduced by the peculiar velocities of the FoF halos.

#### 4 CONCLUSION AND DISCUSSION

In this paper, we extend the well-known SCMS algorithm (Ozertem & Erdogmus 2011; Genovese et al. 2014; Chen et al. 2015b) to recover the cosmic filaments from discrete observations (e.g., galaxies or dark matter halos) on the 2D (RA,DEC) celestial sphere  $\mathbb{S}^2$  and 3D (RA,DEC,z) light cone  $\mathbb{S}^2 \times \mathbb{R}$ , the two nonlinear data space that are commonly encountered in astronomical surveys. Similar to the standard SCMS method in the flat Euclidean space  $\mathbb{R}^d$ , our extended SCMS algorithms in SCONCE, *i.e.*, DirSCMS on  $\mathbb{S}^2$  and DirLinSCMS on  $\mathbb{S}^2 \times \mathbb{R}$ , model the cosmic filaments as one-dimensional density ridges that trace over the regions where the observations are highly concentrated on  $\mathbb{S}^2$  or  $\mathbb{S}^2 \times \mathbb{R}$ . As demonstrated through the cross-shaped filament example in Figure 1 and Figure 3 and the application to SDSS-IV data, our DirSCMS algorithm is invariant to any rotation of the observations on  $\mathbb{S}^2$  and more accurate than the other SCMS typed and DisPerSE methods in approximating the true filamentary structure at the region of high declination. The same advantage also applies to its 3D DirLinSCMS extension. It makes our proposed methods not only useful for the current SDSS data but also capable

of analyzing the data products from other upcoming wide sky surveys, such as EUCLID (Cagliari et al. 2021) and LSST (Ivezić et al. 2019; Bianco et al. 2022), which cover the sky footprint with high declination values. Furthermore, our applications to the FoF halos at  $z = 0$  of the Illustris-3 simulation reveal that our DirLinSCMS algorithm is more robust to the redshift distortions brought by the effects of peculiar velocities.

We summarize the strengths and weaknesses of our extended SCMS methods in Table 2, some of which are inherited from the standard SCMS method (Chen et al. 2015b; Carrón Duque et al. 2022).

We conclude the paper by stating that our proposed DirSCMS algorithm and its estimated cosmic filaments on  $\mathbb{S}^2$  provide a feasible way to identify cosmic voids in both the spectroscopic and photometric redshift surveys. As in Clampitt & Jain (2015), one can project the galaxies within a sufficiently large redshift slice onto the 2D celestial sphere and identify the low-density regions surrounded by the estimated filaments on  $\mathbb{S}^2$  from our DirSCMS algorithm as cosmic voids. This approach is able to seek out cosmic voids with high confidence as long as the light-of-sight width of the redshift slice is at least twice of the redshift resolution (Sánchez et al. 2017). In addition, the cosmic filament model based on density ridges on  $\mathbb{S}^2 \times \mathbb{R}$  and the DirLinSCMS algorithm can be generalized to detect the two-dimensional cosmic sheets/walls with little effort (see Figure 4 in Zhang & Chen 2021c), though the convergence of our DirLinSCMS algorithm could be slower and the yielded two-dimensional structures would be less salient and robust.

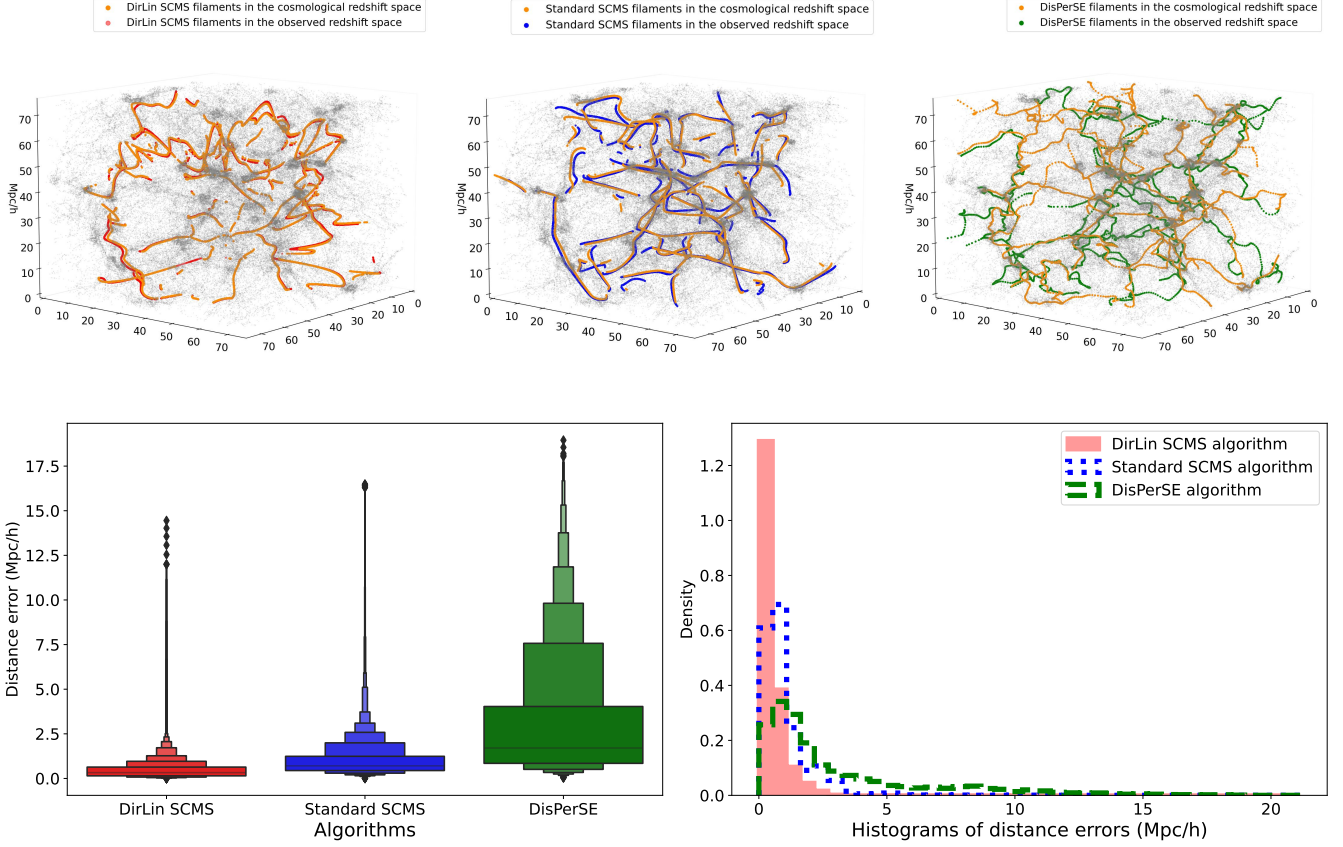


**Figure 6.** Comparisons of filamentary structures in the observed and cosmological redshift spaces detected by our DirLinSCMS, standard SCMS, and DisPerSE algorithms on the FoF halos of Illustris-3 at redshift  $z = 0$ . *Top Row:* the filaments detected by our DirLinSCMS, standard SCMS, and DisPerSE algorithms under the observed and true/cosmological redshift values, respectively. *Bottom Row:* The comparative letter-value plots and histograms of distance errors from the filament detected by each method in the observed redshift space to the one in the cosmological redshift space.

**Table 2.** Pros and cons of our proposed DirSCMS and DirLinSCMS algorithms.

	Strengths	Weaknesses
DirSCMS	<ul style="list-style-type: none"> <li>+ It is more accurate in recovering the filaments on the celestial sphere <math>\mathbb{S}^2</math> than the standard SCMS and DisPerSE algorithms, especially in the regions of high declination.</li> <li>+ It controls the false detection of light-of-sight filaments caused by converting the redshifts to their comoving distances or the finger-of-god effects (Jackson 1972).</li> <li>+ It has a single tuning bandwidth parameter, and the yielded filaments are stable under different choices of the parameter.</li> <li>+ It is easy to implement and fast to execute with parallel programming under the Ray environment (Moritz et al. 2018) provided by our python package SCONCE-SCMS.</li> </ul>	<ul style="list-style-type: none"> <li>– It only recovers the filaments on <math>\mathbb{S}^2</math> (or within some thin redshift slices) and will inevitably miss those light-of-sight structures.</li> </ul>
DirLinSCMS	<ul style="list-style-type: none"> <li>+ It recovers the filaments in the 3D redshift space that are both parallel and perpendicular to the light-of-sight direction.</li> <li>+ The output filaments are relatively robust to the redshift distortions due to the peculiar velocities.</li> </ul>	<ul style="list-style-type: none"> <li>– There are two bandwidth parameters and a step size parameter that need tuning, and the yielded filaments are sensitive to the choices of the bandwidth parameters.</li> <li>– Depending on the step size parameter, it is relatively slower to converge when compared with the DirSCMS algorithm.</li> </ul>
Shared by these two algorithms	<ul style="list-style-type: none"> <li>+ They are adaptive to (either the spherical or conic) survey geometries, rotationally invariant, and independent of the reference coordinate system.</li> <li>+ The yielded filaments are independent of any cosmology and can be used to design the cosmological probes.</li> <li>+ They provide the uncertainty measure for each filamentary point by bootstrap techniques; see Appendix C.</li> </ul>	<ul style="list-style-type: none"> <li>– They determine the filaments (<i>i.e.</i>, estimated density ridges) as a set of discrete realizations; one needs to separate the filaments into individual components and compute their lengths and orientations using other methods.</li> <li>– They only specify the central spines of the filaments but provide no information about their physical widths.</li> </ul>

**ACKNOWLEDGEMENT**

We thank Javier Carrón Duque for implementing the SCMS algorithm with HEALPix on our cross-shaped filament example and Martin A. Fernandez for the helpful discussion about the DisPerSE software.

Funding for the Sloan Digital Sky Survey IV has been provided by the Alfred P. Sloan Foundation, the U.S. Department of Energy Office of Science, and the Participating Institutions.

SDSS-IV acknowledges support and resources from the Center for High Performance Computing at the University of Utah. The SDSS website is [www.sdss.org](http://www.sdss.org).

SDSS-IV is managed by the Astrophysical Research Consortium for the Participating Institutions of the SDSS Collaboration including the Brazilian Participation Group, the Carnegie Institution for Science, Carnegie Mellon University, Center for Astrophysics | Harvard & Smithsonian, the Chilean Participation Group, the French Participation Group, Instituto de Astrofísica de Canarias, The Johns Hopkins University, Kavli Institute for the Physics and Mathematics of the Universe (IPMU) / University of Tokyo, the Korean Participation Group, Lawrence Berkeley National Laboratory, Leibniz Institut für Astrophysik Potsdam (AIP), Max-Planck-Institut für Astronomie (MPIA Heidelberg), Max-Planck-Institut für Astrophysik (MPA Garching), Max-Planck-Institut für Extraterrestrische Physik (MPE), National Astronomical Observatories of China, New Mexico State University, New York University, University of Notre Dame, Observatório Nacional / MCTI, The Ohio State University, Pennsylvania State University, Shanghai Astronomical Observatory, United Kingdom Participation Group, Universidad Nacional Autónoma de México, University of Arizona, University of Colorado Boulder, University of Oxford, University of Portsmouth, University of Utah, University of Virginia, University of Washington, University of Wisconsin, Vanderbilt University, and Yale University.

**DATA AVAILABILITY**

The data and code underlying this paper are available at [https://github.com/zhangyk8/sconce-scms/tree/main/examples/Theory\\_Method\\_Code](https://github.com/zhangyk8/sconce-scms/tree/main/examples/Theory_Method_Code), where the SDSS-IV and Illustris-3 simulation data are obtained from their official websites and post-processed according to our descriptions in the paper.

**REFERENCES**

Aanjaneya M., Chazal F., Chen D., Glisse M., Guibas L. J., Morozov D., 2011, in *Proceedings of the twenty-seventh annual symposium on Computational geometry*. pp 37–46

Abazajian K. N., et al., 2009, *ApJS*, **182**, 543

Abdurro'uf et al., 2021, arXiv e-prints, p. [arXiv:2112.02026](https://arxiv.org/abs/2112.02026)

Absil P.-A., Mahony R., Sepulchre R., 2009, *Optimization algorithms on matrix manifolds*. Princeton University Press

Absil P.-A., Mahony R., Trunpf J., 2013, in *International conference on geometric science of information*. pp 361–368

Ahumada R., et al., 2020, *ApJS*, **249**, 3

Aliyari Ghassabeh Y., Linder T., Takahara G., 2013, *Pattern Recognition*, **46**, 3140

Alpaslan M., et al., 2016, *MNRAS*, **457**, 2287

Aragón-Calvo M. A., Jones B. J. T., van de Weygaert R., van der Hulst J. M., 2007a, *A&A*, **474**, 315

Aragón-Calvo M. A., van de Weygaert R., Jones B. J. T., van der Hulst J. M., 2007b, *ApJ*, **655**, L5

Aragón-Calvo M. A., van de Weygaert R., Jones B. J. T., 2010a, *MNRAS*, **408**, 2163

Aragón-Calvo M. A., Platen E., van de Weygaert R., Szalay A. S., 2010b, *ApJ*, **723**, 364

Arias-Castro E., Mason D., Pelletier B., 2016, *Journal of Machine Learning Research*, **17**, 1

Bai Z., Rao C., Zhao L., 1988, *Journal of Multivariate Analysis*, **27**, 24

Bianco F. B., et al., 2022, *ApJS*, **258**, 1

Bolton A. S., et al., 2012, *AJ*, **144**, 144

Bond J. R., Kofman L., Pogosyan D., 1996, *Nature*, **380**, 603

Bonjean V., Aghanim N., Salomé P., Douspis M., Beelen A., 2018, *A&A*, **609**, A49

Boots B., Sugihara K., Chiu S. N., Okabe A., 2009, *Spatial tessellations: concepts and applications of Voronoi diagrams*. John Wiley & Sons

Boumal N., 2020, Available online, May, 3

Bryant J. J., et al., 2015, *MNRAS*, **447**, 2857

Bundy K., et al., 2015, *ApJ*, **798**, 7

Cagliari M. S., et al., 2021, arXiv e-prints, p. [arXiv:2109.07303](https://arxiv.org/abs/2109.07303)

Carrón Duque J., Migliaccio M., Marinucci D., Vittorio N., 2022, *A&A*, **659**, A166

Cautun M., van de Weygaert R., Jones B. J. T., 2013, *MNRAS*, **429**, 1286

Cautun M., van de Weygaert R., Jones B. J. T., Frenk C. S., 2014, *MNRAS*, **441**, 2923

Chabrier G., 2003, *PASP*, **115**, 763

Chacón J. E., Duong T., Wand M., 2011, *Statistica Sinica*, pp 807–840

Chen Y.-C., 2017, arXiv e-prints, p. [arXiv:1704.03924](https://arxiv.org/abs/1704.03924)

Chen Y.-C., Genovese C. R., Wasserman L., 2014, arXiv e-prints, p. [arXiv:1406.1803](https://arxiv.org/abs/1406.1803)

Chen Y.-C., Genovese C. R., Wasserman L., 2015a, *The Annals of Statistics*, **43**, 1896

Chen Y.-C., Ho S., Freeman P. E., Genovese C. R., Wasserman L., 2015b, *MNRAS*, **454**, 1140

Chen Y.-C., et al., 2015c, *MNRAS*, **454**, 3341

Chen Y.-C., Ho S., Brinkmann J., Freeman P. E., Genovese C. R., Schneider D. P., Wasserman L., 2016, *MNRAS*, **461**, 3896

Chen Y.-C., et al., 2017, *MNRAS*, **466**, 1880

Chen Y.-C., Ho S., Blazek J., He S., Mandelbaum R., Melchior P., Singh S., 2019, *MNRAS*, **485**, 2492

Chen M. C.-Y., et al., 2020, *ApJ*, **891**, 84

Cheng Y., 1995, *IEEE Trans. Pattern Anal. Mach. Intell.*, **17**, 790

Clampitt J., Jain B., 2015, *MNRAS*, **454**, 3357

Clampitt J., Miyatake H., Jain B., Takada M., 2016, *MNRAS*, **457**, 2391

Colless M., et al., 2003, arXiv e-prints, pp [astro-ph/0306581](https://arxiv.org/abs/astro-ph/0306581)

Comaniciu D., Meer P., 2002, *IEEE Transactions on pattern analysis and machine intelligence*, **24**, 603

Comparat J., et al., 2017, arXiv e-prints, p. [arXiv:1711.06575](https://arxiv.org/abs/1711.06575)

Cui W., et al., 2018, *MNRAS*, **480**, 2898

Darvish B., Sobral D., Mobasher B., Scoville N. Z., Best P., Sales L. V., Smail I., 2014, *ApJ*, **796**, 51

Dawson K. S., et al., 2013, *AJ*, **145**, 10

Dawson K. S., et al., 2016, *AJ*, **151**, 44

Driver S. P., et al., 2011, *MNRAS*, **413**, 971

Eberly D., 1996, *Ridges in Image and Data Analysis. Computational Imaging and Vision*, Springer Netherlands

Edelsbrunner H., Letscher D., Zomorodian A., 2000, in *Proceedings 41st annual symposium on foundations of computer science*. pp 454–463

Efron B., 1979, *The Annals of Statistics*, **7**, 1

Efron B., 1981, *Canadian Journal of Statistics*, **9**, 139

Efron B., Tibshirani R. J., 1994, *An introduction to the bootstrap*. CRC press

Falcón-Barroso J., Sánchez-Blázquez P., Vazdekis A., Ricciardelli E., Cardiel N., Cenarro A. J., Gorgas J., Peletier R. F., 2011, *A&A*, **532**, A95

Fernandez M. A., Bird S., Cui Y., 2020, *Phys. Rev. D*, **102**, 043509

Flury B. D., 1990, *SIAM Review*, **32**, 474

Frenk C. S., White S. D. M., 2012, *Annalen der Physik*, **524**, 507

Galárraga-Espinosa D., Aghanim N., Langer M., Gouin C., Malavasi N., 2020, arXiv e-prints,

García-Portugués E., 2013, *Electronic Journal of Statistics*, **7**, 1655

García-Portugués E., Crujeiras R. M., González-Manteiga W., 2013, *Journal of Multivariate Analysis*, **121**, 152

- García-Portugués E., Crujeiras R. M., González-Manteiga W., 2015, *Statistica Sinica*, pp 1207–1229
- Genel S., et al., 2014, *MNRAS*, **445**, 175
- Genovese C. R., Perone-Pacífico M., Verdini I., Wasserman L., 2014, *The Annals of Statistics*, **42**, 1511
- Górski K. M., Hivon E., Banday A. J., Wandelt B. D., Hansen F. K., Reinecke M., Bartelmann M., 2005, *ApJ*, **622**, 759
- Govoni F., et al., 2019, *Science*, **364**, 981
- Guzzo L., et al., 2014, *A&A*, **566**, A108
- Hall P., Watson G., Cabrera J., 1987, *Biometrika*, **74**, 751
- Hearin A. P., et al., 2017, *AJ*, **154**, 190
- Hendel D., Johnston K. V., Patra R. K., Sen B., 2019, *MNRAS*, **486**, 3604
- Hinshaw G., et al., 2013, *ApJS*, **208**, 19
- Hofmann H., Wickham H., Kafadar K., 2017, *Journal of Computational and Graphical Statistics*, **26**, 469
- Horn R. A., Johnson C. R., 2012, *Matrix Analysis*, 2 edn. Cambridge Univ. Press, doi:10.1017/9781139020411
- Inman J., 1849, *Navigation and nautical astronomy, for the use of British seamen*. F. & J. Rivington
- Ivezic Ž., et al., 2019, *ApJ*, **873**, 111
- Jackson J. C., 1972, *MNRAS*, **156**, 1P
- Jones D. H., et al., 2009, *MNRAS*, **399**, 683
- Kafai M., Miao Y., Okada K., 2010, in 2010 IEEE Computer Society Conference on Computer Vision and Pattern Recognition-Workshops. pp 170–177
- Kingman J. F. C., 1993, *Poisson Processes*. Oxford Studies in Probability, Oxford University Press
- Kraljic K., et al., 2020, *MNRAS*, **491**, 4294
- Kreisch D., Pisani A., Villaescusa-Navarro F., Spergel D. N., Wandelt B. D., Hamaus N., Bayer A. E., 2021, arXiv e-prints, p. arXiv:2107.02304
- Kuchner U., et al., 2020, *MNRAS*, **494**, 5473
- Kuchner U., et al., 2022, *MNRAS*, **510**, 581
- Kurz G., Hanebeck U. D., 2015, in 2015 Sensor Data Fusion: Trends, Solutions, Applications (SDF). pp 1–6
- Le Fèvre O., et al., 2005, *A&A*, **439**, 845
- Lecci F., Rinaldo A., Wasserman L., 2014, *Journal of Machine Learning Research*, **15**, 3425
- Ley C., Verdebout T., 2017, *Modern directional statistics*. Chapman and Hall/CRC
- Li X., Hu Z., Wu F., 2007, *Pattern Recognition*, **40**, 1756
- Libeskind N. I., et al., 2018, *MNRAS*, **473**, 1195
- Majewski S. R., et al., 2017, *AJ*, **154**, 94
- Malavasi N., et al., 2017, *MNRAS*, **465**, 3817
- Malavasi N., Aghanim N., Douspis M., Tanimura H., Bonjean V., 2020, arXiv e-prints,
- Malavasi N., Langer M., Aghanim N., Galárraga-Espinosa D., Gouin C., 2022, *A&A*, **658**, A113
- Mardia K., Jupp P., 2000, *Directional Statistics*. Wiley Series in Probability and Statistics, Wiley
- Maritz M. F., 2021, *SIAM Review*, **63**, 395
- Moews B., Argueta Jr J. R., Gieschen A., 2021a, *Decision Support Systems*, **144**, 113518
- Moews B., et al., 2021b, *MNRAS*, **500**, 859
- Moritz P., et al., 2018, in 13th USENIX Symposium on Operating Systems Design and Implementation (OSDI 18). pp 561–577
- Navarro J. F., Frenk C. S., White S. D. M., 1995, *MNRAS*, **275**, 56
- Nelson D., et al., 2015, *Astronomy and Computing*, **13**, 12
- Novikov D., Colombi S., Doré O., 2006, *MNRAS*, **366**, 1201
- Oba S., Kato K., Ishii S., 2005, in Fifth IEEE Symposium on Bioinformatics and Bioengineering (BIBE'05). pp 210–217
- Oliveira M., Crujeiras R. M., Rodríguez-Casal A., 2012, *Computational Statistics & Data Analysis*, **56**, 3898
- Onions J., et al., 2012, *MNRAS*, **423**, 1200
- Ozertem U., Erdogmus D., 2011, *Journal of Machine Learning Research*, **12**, 1249
- Pewsey A., García-Portugués E., 2021, *Test*, **30**, 1
- Pfeifer S., Libeskind N. I., Hoffman Y., Hellwing W. A., Bilicki M., Naidoo K., 2022, arXiv e-prints, p. arXiv:2201.04624
- Poudel A., Heinämäki P., Tempel E., Einasto M., Lietzen H., Nurmi P., 2017, *A&A*, **597**, A86
- Saavedra-Nieves P., María Crujeiras R., 2020, arXiv e-prints, p. arXiv:2009.08915
- Sánchez C., et al., 2017, *MNRAS*, **465**, 746
- Scott D., 2015, *Multivariate Density Estimation: Theory, Practice, and Visualization*. Wiley Series in Probability and Statistics, Wiley
- Scoville N., 2019, *Discrete Morse Theory*. Student Mathematical Library, American Mathematical Society
- Scoville N., et al., 2007, *The Astrophysical Journal Supplement Series*, **172**, 1
- Sheather S. J., 2004, *Statistical science*, pp 588–597
- Sijacki D., Vogelsberger M., Genel S., Springel V., Torrey P., Snyder G. F., Nelson D., Hernquist L., 2015, *MNRAS*, **452**, 575
- Silverman B., Young G., 1987, *Biometrika*, **74**, 469
- Sousbie T., 2011, *MNRAS*, **414**, 350
- Sousbie T., Pichon C., Kawahara H., 2011, *MNRAS*, **414**, 384
- Springel V., White S. D. M., Tormen G., Kauffmann G., 2001, *MNRAS*, **328**, 726
- Springel V., et al., 2005, *Nature*, **435**, 629
- Taylor C. C., 2008, *Computational Statistics & Data Analysis*, **52**, 3493
- Tempel E., Stoica R. S., Martínez V. J., Liivamägi L. J., Castellan G., Saar E., 2014, *MNRAS*, **438**, 3465
- Turner E. L., Gott J. R. I., 1976, *ApJS*, **32**, 409
- Ulrich G., 1984, *Journal of the Royal Statistical Society. Series C (Applied Statistics)*, **33**, 158
- Vogelsberger M., et al., 2014a, *MNRAS*, **444**, 1518
- Vogelsberger M., et al., 2014b, *Nature*, **509**, 177
- Vogelsberger M., Marinacci F., Torrey P., Puchwein E., 2020, *Nature Reviews Physics*, **2**, 42
- Wechsler R. H., Tinker J. L., 2018, *ARA&A*, **56**, 435
- Weigel A. K., Schawinski K., Bruderer C., 2016, *MNRAS*, **459**, 2150
- Wilkinson D. M., Maraston C., Goddard D., Thomas D., Parikh T., 2017, *MNRAS*, **472**, 4297
- Wood A. T., 1994, *Communications in Statistics - Simulation and Computation*, **23**, 157
- York D. G., et al., 2000, *AJ*, **120**, 1579
- Zeldovich I. B., Einasto J., Shandarin S. F., 1982, *Nature*, **300**, 407
- Zhang Y., Chen Y.-C., 2021a, arXiv e-prints, p. arXiv:2101.10058
- Zhang Y., Chen Y.-C., 2021b, arXiv e-prints, p. arXiv:2104.14977
- Zhang Y., Chen Y.-C., 2021c, arXiv e-prints, p. arXiv:2110.08505
- Zhang Y., Chen Y.-C., 2021d, *Journal of Machine Learning Research*, **22**, 1
- Zhang Y., Yang X., Faltenbacher A., Springel V., Lin W., Wang H., 2009, *ApJ*, **706**, 747
- Zhang Y., Yang X., Wang H., Wang L., Mo H. J., van den Bosch F. C., 2013, *ApJ*, **779**, 160
- Zhao L., Wu C., 2001, *Science in China A: Mathematics*, **44**, 474
- van de Weygaert R., Schaap W., 2009, in Martínez V. J., Saar E., Martínez-González E., Pons-Bordería M. J., eds., Vol. 665, *Data Analysis in Cosmology*. pp 291–413

## APPENDIX A: RIEMANNIAN GRADIENT AND HESSIAN

Given a smooth function  $f$  on a Riemannian manifold  $\mathcal{M}$ , where  $\mathcal{M}$  is the celestial sphere  $\mathbb{S}^2$  or 3D light cone  $\mathbb{S}^2 \times \mathbb{R}$  in our cosmic filament detection scenario, its *Riemannian gradient*  $\text{grad } f(\mathbf{x})$  is defined as a unique vector in the tangent space  $T_{\mathbf{x}}$  such that

$$df_{\mathbf{x}}(\mathbf{v}) = \langle \text{grad } f(\mathbf{x}), \mathbf{v} \rangle_{\mathbf{x}} \quad (\text{A1})$$

for any  $\mathbf{v} \in T_{\mathbf{x}}$ , where  $df_{\mathbf{x}}(\mathbf{v})$  is the directional derivative (or more technically, the differential) of  $f$  at  $\mathbf{x} \in \mathcal{M}$  along the tangent direction  $\mathbf{v}$  and  $\langle \cdot, \cdot \rangle_{\mathbf{x}}$  is the Riemannian metric.

The *Riemannian Hessian*  $\mathcal{H}f(\mathbf{x})$  at any point  $\mathbf{x} \in \mathcal{M}$  is the linear map from the tangent space  $T_{\mathbf{x}}$  to itself as:

$$\mathcal{H}f(\mathbf{x})[\mathbf{u}] = \bar{\nabla}_{\mathbf{u}} \text{grad } f(\mathbf{x}) \quad (\text{A2})$$

for any tangent vector  $\mathbf{u} \in T_{\mathbf{x}}$ , where  $\bar{\nabla}_{\mathbf{u}}$  is the Riemannian connection on  $\mathcal{M}$ . More details about the definitions of Riemannian gradient and Hessian on a general manifold can be found in, e.g., [Absil et al. \(2009\)](#) or [Boumal \(2020\)](#).

### A1 On the Celestial sphere $\mathbb{S}^2$

While it is mathematically involved to calculate the Riemannian gradient and Hessian directly from the definitions (A1) and (A2), we can view the celestial sphere  $\mathbb{S}^2$  as a 2D (Riemannian) submanifold in the ambient Euclidean space  $\mathbb{R}^3$ . After a proper extension of  $f$  from  $\mathbb{S}^2$  to its neighborhood in  $\mathbb{R}^3$ , the Riemannian gradient and Hessian of  $f$  on  $\mathbb{S}^2$  are related to the regular gradient  $\nabla f(\mathbf{x}) \in \mathbb{R}^3$  and Hessian  $\nabla\nabla f(\mathbf{x}) \in \mathbb{R}^{3 \times 3}$  in the ambient Euclidean space  $\mathbb{R}^3$  as ([Absil et al. 2009, 2013; Zhang & Chen 2021d](#)):

$$\begin{aligned} \text{grad } f(\mathbf{x}) &= (\mathbf{I}_3 - \mathbf{x}\mathbf{x}^T) \nabla f(\mathbf{x}), \\ \mathcal{H}f(\mathbf{x}) &= (\mathbf{I}_3 - \mathbf{x}\mathbf{x}^T) \left[ \nabla\nabla f(\mathbf{x}) - \mathbf{x}^T \nabla f(\mathbf{x}) \cdot \mathbf{I}_3 \right] (\mathbf{I}_3 - \mathbf{x}\mathbf{x}^T), \end{aligned} \quad (\text{A3})$$

where  $\mathbf{I}_3 \in \mathbb{R}^{3 \times 3}$  is the identity matrix. Since the eigenvectors  $\mathbf{v}_i(\mathbf{x}), i = 1, 2$  of  $\mathcal{H}f(\mathbf{x})$  within the tangent space  $T_{\mathbf{x}}$  are orthogonal to  $\mathbf{x}$  by definition, it follows from (A3) that

$$\mathbf{v}_i(\mathbf{x})^T \text{grad } f(\mathbf{x}) = \mathbf{v}_i(\mathbf{x})^T (\mathbf{I}_3 - \mathbf{x}\mathbf{x}^T) \nabla f(\mathbf{x}) = \mathbf{v}_i(\mathbf{x})^T \nabla f(\mathbf{x})$$

for  $i = 1, 2$ , and we obtain an equivalent definition of the (directional) density ridge of  $f$  to (4) as:

$$R(f) = \left\{ \mathbf{x} \in \mathbb{S}^2 : \mathbf{v}_2(\mathbf{x})^T \nabla f(\mathbf{x}) = \mathbf{0}, \lambda_2(\mathbf{x}) < 0 \right\}. \quad (\text{A4})$$

The definition (4) or (A4) of density ridge  $R(f)$  can also be arguably generalized to the sphere with arbitrary dimension and even any smooth density function on a general manifold; see Section 4.1 in [Zhang & Chen \(2021b\)](#).

### A2 On the 3D Light Cone $\mathbb{S}^2 \times \mathbb{R}$

Similarly, we regard the 3D light cone  $\mathbb{S}^2 \times \mathbb{R}$  as a submanifold of its ambient Euclidean space  $\mathbb{R}^4$  and compute the Riemannian gradient and Hessian of  $f_{dl}$  (after a proper extension) according to the regular gradient  $\nabla f_{dl}(\mathbf{x}, z) \in \mathbb{R}^4$  and  $\nabla\nabla f_{dl}(\mathbf{x}, z) \in \mathbb{R}^{4 \times 4}$  as:

$$\begin{aligned} \text{grad } f_{dl}(\mathbf{x}, z) &= \mathcal{P}_{\mathbf{x}} \nabla f_{dl}(\mathbf{x}, z), \\ \mathcal{H}f_{dl}(\mathbf{x}, z) &= \mathcal{P}_{\mathbf{x}} \left[ \nabla\nabla f_{dl}(\mathbf{x}, z) - \begin{pmatrix} \mathbf{x}^T \nabla_{\mathbf{x}} f_{dl}(\mathbf{x}, z) & \mathbf{0} \\ \mathbf{0}^T & 0 \end{pmatrix} \right] \mathcal{P}_{\mathbf{x}}, \end{aligned} \quad (\text{A5})$$

where  $\mathcal{P}_{\mathbf{x}} = \begin{pmatrix} \mathbf{I}_3 - \mathbf{x}\mathbf{x}^T & \mathbf{0} \\ \mathbf{0}^T & 1 \end{pmatrix} \in \mathbb{R}^{4 \times 4}$  is the projection matrix,  $\mathbf{0} = (0, 0, 0)^T \in \mathbb{R}^3$  is a zero vector, and  $\nabla f_{dl}(\mathbf{x}, z) = \begin{pmatrix} \nabla_{\mathbf{x}} f_{dl}(\mathbf{x}) \\ \nabla_z f_{dl}(\mathbf{x}) \end{pmatrix} \in \mathbb{R}^4$ . Likewise, given that the columns of  $V_{dl}(\mathbf{x}, z) = [\mathbf{v}_{dl,2}(\mathbf{x}, z), \mathbf{v}_{dl,3}(\mathbf{x}, z)] \in \mathbb{R}^{4 \times 2}$  derived from the eigenvectors of  $\mathcal{H}f_{dl}(\mathbf{x}, z)$  within the tangent space  $T_{(\mathbf{x}, z)}$  of  $\mathbb{S}^2 \times \mathbb{R}$  are orthogonal to  $(\mathbf{x}, z)$  by definition, we have that

$$V_{dl}(\mathbf{x}, z)^T \text{grad } f_{dl}(\mathbf{x}, z) = V_{dl}(\mathbf{x}, z)^T \nabla f_{dl}(\mathbf{x}, z)$$

and an equivalent form for the density ridge (9) on  $\mathbb{S}^2 \times \mathbb{R}$  as:

$$R(f_{dl}) = \left\{ (\mathbf{x}, z) \in \mathbb{S}^2 \times \mathbb{R} : V_{dl}(\mathbf{x}, z)^T \nabla f_{dl}(\mathbf{x}, z) = \mathbf{0}, \lambda_{dl,2}(\mathbf{x}, z) < 0 \right\}. \quad (\text{A6})$$

## APPENDIX B: DETAILED DESCRIPTIONS OF OUR PROPOSED ALGORITHMS IN SCNCE

In Section 2.2 and Section 2.3, we have introduced our extended SCMS algorithms on  $\mathbb{S}^2$  and  $\mathbb{S}^2 \times \mathbb{R}$ , especially their key iterative formulae (7) and (10). Here, we provide additional details on their implementations in practice, including the computations of estimated Riemannian Hessian matrices and stopping criteria. Additionally, we discuss how to incorporate stellar properties into the filament detection process with our DirSCMS algorithm in Appendix B2 and delineate the algorithmic procedures for seeking out the cosmic nodes in Appendix B4.

### B1 DirSCMS Algorithm on $\mathbb{S}^2$

The implementation of our DirSCMS algorithm requires the calculations of the estimated Riemannian Hessian  $\mathcal{H}\hat{f}(\mathbf{x})$  from the directional KDE (5) and its eigenvectors. Based on (A3), the estimated Riemannian Hessian  $\mathcal{H}\hat{f}(\mathbf{x})$  has its formula as:

$$\begin{aligned} \mathcal{H}\hat{f}(\mathbf{x}) &= \frac{C_L(b)}{nb^2} (\mathbf{I}_3 - \mathbf{x}\mathbf{x}^T) \left[ \frac{1}{b^2} \sum_{i=1}^n \mathbf{X}_i \mathbf{X}_i^T \cdot L'' \left( \frac{1 - \mathbf{X}_i^T \mathbf{x}}{b^2} \right) \right. \\ &\quad \left. + \sum_{i=1}^n \mathbf{X}_i^T \mathbf{x} \cdot \mathbf{I}_3 \cdot L' \left( \frac{1 - \mathbf{X}_i^T \mathbf{x}}{b^2} \right) \right] (\mathbf{I}_3 - \mathbf{x}\mathbf{x}^T), \end{aligned} \quad (\text{B1})$$

and we compute its last eigenvector  $\hat{\mathbf{v}}_2(\mathbf{x})$  within the tangent space  $T_{\mathbf{x}}$  of  $\mathbb{S}^2$  via the spectral decomposition ([Horn & Johnson 2012](#)). We run the DirSCMS iterative formula (7) in Section 2.2.2 or its general form (B5) in Appendix B2 until

$$\left\| \hat{\mathbf{v}}_2(\mathbf{x})^T \text{grad } \hat{f}(\mathbf{x}) \right\|_2 = \left\| \hat{\mathbf{v}}_2(\mathbf{x})^T \nabla \hat{f}(\mathbf{x}) \right\|_2 \leq \epsilon,$$

where  $\epsilon > 0$  is a precision level for stopping the algorithm. Notice also that we leverage the normalized gradient

$$\frac{\nabla \hat{f}(\mathbf{x}^{(t)})}{\left\| \nabla \hat{f}(\mathbf{x}^{(t)}) \right\|_2} = \frac{\sum_{i=1}^n \mathbf{X}_i L' \left( \frac{1 - \mathbf{X}_i^T \mathbf{x}^{(t)}}{b^2} \right)}{\left\| \sum_{i=1}^n \mathbf{X}_i L' \left( \frac{1 - \mathbf{X}_i^T \mathbf{x}^{(t)}}{b^2} \right) \right\|_2}$$

in our design of the DirSCMS iteration (7) instead of the standard gradient  $\nabla \hat{f}(\mathbf{x}^{(t)})$  in pursuit of a faster convergence among low-density regions ([Zhang & Chen 2021b](#)).

We summarize the full filament detection procedures on  $\mathbb{S}^2$  in Algorithm 1. Given that the observational data always contain a lot of noise, we incorporate an extra denoising step before applying the DirSCMS iteration (7) in our filament detection procedures on  $\mathbb{S}^2$ ; see Step 2 in Algorithm 1. One can follow the discussion in Appendix A of [Chen et al. \(2015b\)](#) to select the denoising threshold  $\tau$ . In our applications of the DirSCMS algorithm, we use the von Mises kernel, leading to the equation  $L''(r) = -L'(r) = L(r) = e^{-r}$ .

### B2 Weighted DirSCMS Algorithm on $\mathbb{S}^2$

In statistical parlance, an astronomical survey can be understood as a marked point process, where the marks are represented by stellar properties of the observed galaxies or simulated dark matter halos ([Ahumada et al. 2020; Vogelsberger et al. 2020](#)). These extra properties of the astronomical objects are not only useful in analyzing its intrinsic evolution but also facilitate the estimation of the underlying matter distribution and its filamentary structures. For instance, [Kuchner et al. \(2020\)](#) has demonstrated by mock galaxy samples that

**Algorithm 1** Cosmic Filament Detection on the Celestial Sphere  $\mathbb{S}^2$  via the DirSCMS Algorithm

**Input:**

- The data sample with the Cartesian coordinate  $\mathcal{D} = \{X_1, \dots, X_n\}$  on  $\mathbb{S}^2$ .
- The smoothing bandwidth  $b > 0$ , threshold value  $\tau > 0$ , precision level  $\epsilon > 0$  for stopping the algorithm, and a suitable mesh  $\mathcal{M}_D \subset \mathbb{S}^2$  of initial points covering the region of interest.

**Step 1:** Compute the estimated density function  $\hat{f}(\mathbf{x}) = \frac{C_L(b)}{n} \sum_{i=1}^n L\left(\frac{1-\mathbf{x}^T X_i}{b^2}\right)$  or more generally, via (B2), on the data sample  $\mathcal{D}$ .

**Step 2:** Remove  $X' \in \mathcal{D}$  whenever  $\hat{f}(X') < \tau$ . Denote the remaining data sample by  $\tilde{\mathcal{D}}$ .

**Step 3:** For each  $\mathbf{x}^{(0)} \in \mathcal{M}_D$ , iterate the following procedure until convergence:

**while**  $\left\| \hat{\mathbf{v}}_2(\mathbf{x}^{(t)})^T \nabla \hat{f}(\mathbf{x}^{(t)}) \right\|_2 > \epsilon$  **do:** (At iteration step  $t$ )

**Step 3-1:** Compute the estimated Riemannian Hessian matrix  $\mathcal{H}\hat{f}(\mathbf{x}^{(t)})$  as in (B1) or more generally, (B6).

**Step 3-2:** Compute  $\hat{\mathbf{v}}_2(\mathbf{x}^{(t)})$  as the last eigenvector of  $\mathcal{H}\hat{f}(\mathbf{x}^{(t)})$  inside the tangent space  $T_{\mathbf{x}^{(t)}}$  of  $\mathbb{S}^2$  via the spectral decomposition.

**Step 3-3:** Update  $\tilde{\mathbf{x}}^{(t+1)} \leftarrow \mathbf{x}^{(t)} - \hat{\mathbf{v}}_2(\mathbf{x}^{(t)}) \hat{\mathbf{v}}_2(\mathbf{x}^{(t)})^T \left[ \frac{\sum_{i=1}^n X_i L' \left( \frac{1-X_i^T \mathbf{x}^{(t)}}{b^2} \right)}{\left\| \sum_{i=1}^n X_i L' \left( \frac{1-X_i^T \mathbf{x}^{(t)}}{b^2} \right) \right\|_2} \right]$  or more generally, via (B5).

**Step 3-4:** Standardize  $\tilde{\mathbf{x}}^{(t+1)}$  as  $\mathbf{x}^{(t+1)} \leftarrow \frac{\tilde{\mathbf{x}}^{(t+1)}}{\|\tilde{\mathbf{x}}^{(t+1)}\|_2}$ .

**end while**

**Output:** The estimated filament set (or density ridge)  $R(\hat{f})$  on  $\mathbb{S}^2$  represented by the collection of converged points.

the filaments can be better recovered by the mass-weighted galaxies. Here, we describe how to generalize our proposed DirSCMS algorithm to incorporate a given property of interest into the filament estimation on  $\mathbb{S}^2$ .

### B2.1 Methodology

Assume that the data are  $(X_1, Y_1), \dots, (X_n, Y_n)$  sampled from a (directional-linear) density function  $f_{dl}(\mathbf{x}, y)$  on  $\mathbb{S}^2 \times \mathbb{R}$ , where  $X_i, i = 1, \dots, n$  are Cartesian coordinates of their locations on  $\mathbb{S}^2$  and  $Y_i, i = 1, \dots, n$  are their associated stellar properties of interest. Instead of directly estimating the density function  $f_{dl}$ , which has been discussed in Section 2.3, we utilize  $Y_i, i = 1, \dots, n$  as the weights of the directional KDE (5) to construct an estimator as:

$$\hat{f}_g(\mathbf{x}) = C_L(b) \sum_{i=1}^n Y_i \cdot L\left(\frac{1-\mathbf{x}^T X_i}{b^2}\right), \quad (\text{B2})$$

where  $L(\cdot)$  and  $b$  are the directional kernel function and smoothing bandwidth parameter, respectively. This weighted estimator better approximates the matter density function (up to a scaled factor) by, e.g., placing more weights on the heavier objects. The intended estimand of (B2), however, is no longer a probability density function but a *generalized density function* on  $\mathbb{S}^2$  as (Chen et al. 2014):

$$f_g(\mathbf{x}) = \int_{\mathbb{R}} y \cdot f_{dl}(\mathbf{x}, y) dy = f(\mathbf{x}) \cdot \mathbb{E}(Y_i | X_i = \mathbf{x}), \quad (\text{B3})$$

where  $f(\mathbf{x})$  is the marginal density function of  $\{X_i\}_{i=1}^n$  on  $\mathbb{S}^2$  and  $\mathbb{E}(Y_i | X_i = \mathbf{x})$  is the conditional expectation of  $Y_i$  given  $X_i = \mathbf{x}$ . This generalized density function  $f_g$  is also known as the intensity function in the domain of spatial (marked) point process (Kingman 1993). The density ridge or cosmic filament model based on  $f_g$  is defined similarly as:

$$R(f_g) = \left\{ \mathbf{x} \in \mathbb{S}^2 : \mathbf{v}_{g,2}(\mathbf{x})^T \text{grad } f_g(\mathbf{x}) = \mathbf{0}, \lambda_{g,2}(\mathbf{x}) < 0 \right\} \quad (\text{B4})$$

and can be also estimated by the plug-in estimator  $R(\hat{f}_g)$ , where the Riemannian Hessian  $\mathcal{H}f_g(\mathbf{x})$  has its eigen-system as  $\{(\mathbf{v}_{g,i}(\mathbf{x}), \lambda_{g,i}(\mathbf{x})) \text{ for } i = 1, 2 \text{ with } \lambda_{g,1}(\mathbf{x}) \geq \lambda_{g,2}(\mathbf{x})\}$  in the tangent space  $T_{\mathbf{x}}$  at  $\mathbf{x} \in \mathbb{S}^2$ . Identifying the (estimated) density ridges

of the generalized density function is analogous to our DirSCMS algorithm in Section 2.2.2 but with a more general SCMS iteration as:

$$\tilde{\mathbf{x}}^{(t+1)} \leftarrow \mathbf{x}^{(t)} - \hat{\mathbf{v}}_{g,2}(\mathbf{x}^{(t)}) \hat{\mathbf{v}}_{g,2}(\mathbf{x}^{(t)})^T \left[ \frac{\sum_{i=1}^n Y_i X_i L' \left( \frac{1-X_i^T \mathbf{x}^{(t)}}{b^2} \right)}{\left\| \sum_{i=1}^n Y_i X_i L' \left( \frac{1-X_i^T \mathbf{x}^{(t)}}{b^2} \right) \right\|_2} \right] \quad (\text{B5})$$

and  $\mathbf{x}^{(t+1)} \leftarrow \frac{\tilde{\mathbf{x}}^{(t+1)}}{\|\tilde{\mathbf{x}}^{(t+1)}\|_2}$ , where  $\hat{\mathbf{v}}_{g,2}(\mathbf{x})$  is the last eigenvector of the estimated Riemannian Hessian

$$\mathcal{H}\hat{f}_g(\mathbf{x}) = \frac{C_L(b)}{b^2} (\mathbf{I}_3 - \mathbf{x}\mathbf{x}^T) \left[ \frac{1}{b^2} \sum_{i=1}^n Y_i X_i X_i^T \cdot L'' \left( \frac{1-X_i^T \mathbf{x}}{b^2} \right) + \sum_{i=1}^n Y_i X_i^T \mathbf{x} \cdot \mathbf{I}_3 \cdot L' \left( \frac{1-X_i^T \mathbf{x}}{b^2} \right) \right] (\mathbf{I}_3 - \mathbf{x}\mathbf{x}^T) \quad (\text{B6})$$

inside the tangent space  $T_{\mathbf{x}}$ . Notice that the weighted DirSCMS algorithm (B5) reduces to the usual DirSCMS algorithm (7) when all the weights  $Y_1, \dots, Y_n$  are equal.

### B2.2 Comparison Between the Unweighted and Mass-Weighted DirSCMS Algorithms on SDSS-IV Data

Recent studies on simulation and survey data suggest that the galaxies tend to be redder and heavier in their stellar masses when they are closer to filaments (Alpaslan et al. 2016; Malavasi et al. 2017; Chen et al. 2017). While other stellar properties of galaxies, such as the luminosity and star formation rate, are also correlated with their proximity to the nearby filaments, we showcase how the stellar mass properties can influence the cosmic filament detection with our DirSCMS algorithm as an example here because the stellar mass property and its estimation function serve as a key measure for other stellar properties (Weigel et al. 2016).

To this end, we take another thin redshift slice  $0.06 \leq z < 0.065$  from the SDSS-IV galactic data described in Section 3.2. The stellar

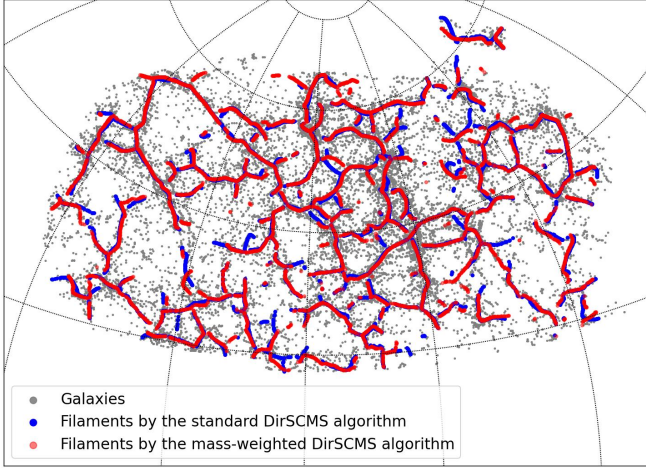
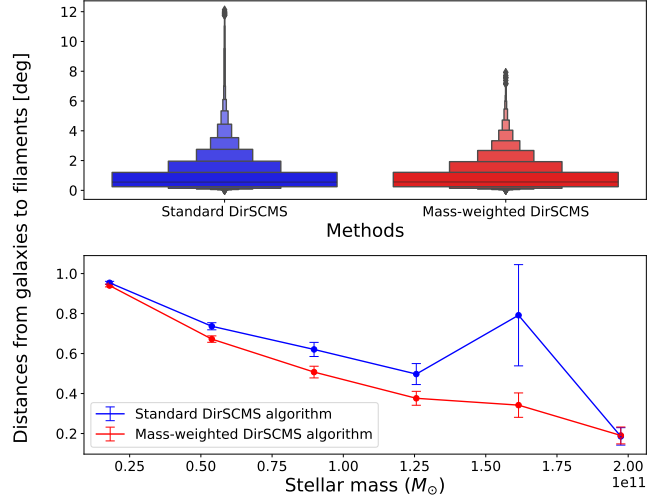


**Figure B1.** Comparisons of cosmic filaments detected by the usual DirSCMS (Algorithm 1) and mass-weighted DirSCMS (Section B2) algorithms on a thin redshift slice SDSS-IV galactic data ( $0.06 \leq z < 0.065$ ). *Left:* The filaments detected by our DirSCMS algorithm on galaxies with and without the information of estimated stellar masses. *Top Right:* The letter-value plots of the distances from galaxies to the two sets of filaments. *Bottom Right:* The correlation between stellar masses of galaxies and their distances to the two sets of filaments on  $\mathbb{S}^2$ .

masses of selected galaxies are obtained from SDSS spectra by the FIREFLY (Fitting ItErativEly For Likelihood analYsis) stellar population model (Wilkinson et al. 2017; Comparat et al. 2017). This model estimates the stellar properties by leveraging the Chabrier (2003) stellar initial mass function under the input stellar library MILES (Falc3n-Barroso et al. 2011). We access the estimated stellar masses from the FIREFLY value added catalog<sup>8</sup>, among which a tiny portion ( $\sim 6.36\%$ ) of stellar masses are missing in our selected redshift slice. For simplicity, we subset those galaxies with non-missing estimated stellar masses by the FIREFLY model in the North Galactic Cap ( $100^\circ < \text{RA} < 270^\circ$ ,  $-5^\circ < \text{DEC} < 70^\circ$ ), leading to a galactic dataset on  $\mathbb{S}^2$  with 25,207 observations.

Both the usual DirSCMS method (Algorithm 1 with an equal weight for each observation) and mass-weighted DirSCMS algorithm are applied to the above galactic dataset on  $\mathbb{S}^2$ , whose bandwidth parameter is chosen using (14) with  $B_0 = 0.25$ . The resulting filaments are presented in Figure B1, in which they do exhibit non-negligible differences in terms of their structures and distances from the galaxies. On the one hand, the galaxies within the selected redshift slice are, on average, closer to the filaments detected by the mass-weighted DirSCMS algorithm than the standard one. Specifically, the galaxies within mass groups from  $5 \times 10^{10} M_\odot$  to  $1.6 \times 10^{11} M_\odot$  are statistically closer to the mass-weighted filaments than its equally weighted counterparts. It provides some additional supporting evidence based on survey data other than simulation data in Kuchner et al. (2020) that it is beneficial to detect cosmic filaments with mass-weighted galaxies. Nevertheless, estimating the stellar mass properties is never easy on observed galaxies, so it is still more common to recover the filaments by assuming an equal weight for each galaxy on survey data. Furthermore, we observe from the decreasing trend in the bottom right panel of Figure B1 that the galaxies around the two filaments tend to be more massive than the ones that are farther away from the filaments. This result, to some extent, supports the previous claim about the correlation between the stellar mass and proximity to filaments.

<sup>8</sup> The data can be downloaded at <https://www.sdss.org/dr17/spectro/eboss-firefly-value-added-catalog>.



### B3 DirLinSCMS Algorithm on $\mathbb{S}^2 \times \mathbb{R}$

The full procedures of detecting cosmic filaments in  $\mathbb{S}^2 \times \mathbb{R}$  via our DirLinSCMS algorithm is essentially identical to Algorithm 1, except that we estimate the density function via (8) and compute its Riemannian Hessian  $\mathcal{H}\widehat{f}_{dl}(\mathbf{x}, z)$  as:

$$\mathcal{H}\widehat{f}_{dl}(\mathbf{x}, z) = \begin{pmatrix} \mathcal{H}_{xx}\widehat{f}_{dl}(\mathbf{x}, z) & \mathcal{H}_{xz}\widehat{f}_{dl}(\mathbf{x}, z) \\ \left[\mathcal{H}_{xz}\widehat{f}_{dl}(\mathbf{x}, z)\right]^T & \mathcal{H}_{zz}\widehat{f}_{dl}(\mathbf{x}, z) \end{pmatrix} \in \mathbb{R}^{4 \times 4}, \quad (\text{B7})$$

where

$$\begin{aligned} \mathcal{H}_{xx}\widehat{f}_{dl}(\mathbf{x}, z) &= \frac{C_L(b_1)}{nb_1^2 b_2} \left( I_3 - \mathbf{x}\mathbf{x}^T \right) \sum_{i=1}^n \left[ \frac{X_i X_i^T}{b_1^2} L'' \left( \frac{1 - X_i^T \mathbf{x}}{b_1} \right) K \left( \left\| \frac{z - Z_i}{b_2} \right\|_2^2 \right) \right. \\ &\quad \left. + \sum_{i=1}^n \mathbf{x}^T X_i \cdot I_3 \cdot L' \left( \frac{1 - X_i^T \mathbf{x}}{b_1} \right) K \left( \left\| \frac{z - Z_i}{b_2} \right\|_2^2 \right) \right] \left( I_3 - \mathbf{x}\mathbf{x}^T \right), \\ \mathcal{H}_{xz}\widehat{f}_{dl}(\mathbf{x}, z) &= -\frac{2C_L(b_1)}{nb_1^2 b_2^3} \sum_{i=1}^n (z - Z_i) X_i \cdot L' \left( \frac{1 - X_i^T \mathbf{x}}{b_1} \right) K' \left( \left\| \frac{z - Z_i}{b_2} \right\|_2^2 \right), \\ \mathcal{H}_{zz}\widehat{f}_{dl}(z, z) &= \frac{2C_L(b_1)}{nb_2^3} \sum_{i=1}^n \left[ L \left( \frac{1 - X_i^T \mathbf{x}}{b_1} \right) K' \left( \left\| \frac{z - Z_i}{b_2} \right\|_2^2 \right) \right. \\ &\quad \left. + \sum_{i=1}^n \frac{2(z - Z_i)^2}{b_2^2} \cdot L \left( \frac{1 - X_i^T \mathbf{x}}{b_1} \right) K'' \left( \left\| \frac{z - Z_i}{b_2} \right\|_2^2 \right) \right]. \end{aligned}$$

Steps 3-3 and 3-4 in Algorithm 1 will be replaced by (10) as well.

Different from our DirSCMS algorithm on the celestial sphere  $\mathbb{S}^2$ , which is controlled by a single bandwidth parameter, the performance of our DirLinSCMS algorithm on the 3D light cone  $\mathbb{S}^2 \times \mathbb{R}$  relies on the proper tuning of bandwidth parameters for both the directional and linear data components. Here, we demonstrate how the estimated filaments by our DirLinSCMS algorithm change under different combinations of the directional and linear bandwidth parameters  $b_1, b_2$  through the Illustris-3 FoF halo data at redshift  $z = 0$  in Section 3.3.

The bandwidth parameter  $b_1$  for the directional data part is selected via (14) and  $b_2$  for the linear data part is chosen by (13) with  $d = 1$ . We vary their values by changing the scale factors  $B_0, A_0$  in (14) and (13). To ensure that  $b_1, b_2$  are properly balanced on the Illustris FoF halo data, we consider 21 combinations of  $(A_0, B_0)$  as specified in Figure B2, under which the bandwidth parameters  $b_1, b_2$  are roughly of the same value when  $(A_0, B_0) = (80, 1), (60, 0.75),$  and  $(40, 0.5)$ . As in Section 3.3, we compute the distance errors from the filament by our DirLinSCMS algorithm in the observed redshift space to the one in the cosmological redshift space under each combination of the directional and linear bandwidth parameters. The 3D plots in Figure B2 reveal that the filamentary structures by our DirLinSCMS algorithm are sensitive to the choices of its two bandwidth parameters. Their distance errors under the redshift distortions, however, remain steadily small under all these combinations of the directional and linear bandwidths; see the fourth row of Figure B2. For better comparison, we also compute the distance error distributions under the redshift distortions for the FoF halo themselves, the standard SCMS algorithm under different choices of its single bandwidth parameter, and DisPerSE with various persistence ratio thresholds. Compared with our DirLinSCMS algorithm, the distance error distributions for the standard SCMS algorithm and DisPerSE change more dramatically under different choices of their tuning parameters and have average values larger than the mean distance errors embraced by the FoF halos themselves.

Another criterion to judge the quality of an estimated filamentary structure is whether the filament traces out the high-density regions of the observed data. We quantify this criterion by calculating the number of FoF halos,  $N_h$ , within a  $3 \text{ Mpc}/h$  neighborhood sphere centered at each point of the estimated filament in the observed redshift space. The quantity  $N_h$  is further normalized by the volume of the neighborhood sphere  $V_n = \frac{4\pi}{3} (3 \text{ Mpc}/h)^3$  to obtain the halo number density  $N_H/V_n$  in unit of  $(\text{Mpc}/h)^{-3}$  for each filamentary point. The results are presented at the fifth row of Figure B2. Compared with the standard SCMS and DisPerSE algorithms, our DirLinSCMS algorithm produced some filamentary structure with relatively low halo number densities. This undesired result for our DirLinSCMS algorithm may be due to the fact that FoF halos of the Illustris simulation are designed in a regular 3D cube and do not inherently embrace a conic geometry. In the future, we are planning to apply our DirLinSCMS algorithm to other survey data, where each object is originally observed in the  $(\text{RA}, \text{DEC}, z)$  light cone space, and further access the utility of our DirLinSCMS algorithm.

#### B4 Computation of Cosmic Nodes

We know from Section 2.4 that our filament model based on density ridges is a natural host of two types of cosmic nodes, local modes and knots. Here, we delineate the practical algorithms to seek out these two types of cosmic nodes on both the celestial sphere  $\mathbb{S}^2$  and the 3D light cone  $\mathbb{S}^2 \times \mathbb{R}$ .

• **Identifying local modes.** To obtain the local modes of directional (5) or directional-linear KDE (8), the mean shift method (Oba et al. 2005; Kafai et al. 2010; Zhang & Chen 2021d; Zhang & Chen 2021c), the prototype of the SCMS algorithm, is an ideal choice. The mean shift algorithm updates an iterative point  $\mathbf{x}^{(t)} \in \mathbb{S}^2$  or  $(\mathbf{x}^{(t)}, z^{(t)}) \in \mathbb{S}^2 \times \mathbb{R}$  at step  $t$  with a fixed-point equation as:

$$\bullet \text{ Spherical case : } \mathbf{x}^{(t+1)} \leftarrow - \frac{\sum_{i=1}^n X_i L' \left( \frac{1 - X_i^T \mathbf{x}^{(t)}}{b^2} \right)}{\left\| \sum_{i=1}^n X_i L' \left( \frac{1 - X_i^T \mathbf{x}^{(t)}}{b^2} \right) \right\|_2}, \quad (\text{B8})$$

$$\bullet \text{ Conic case : } \begin{pmatrix} \bar{\mathbf{x}}^{(t+1)} \\ z^{(t+1)} \end{pmatrix} \leftarrow \begin{pmatrix} \frac{\sum_{i=1}^n X_i \cdot L' \left( \frac{1 - X_i^T \mathbf{x}^{(t)}}{b_1} \right) K \left( \left\| \frac{z^{(t)} - Z_i}{b_2} \right\|_2 \right)^2}{\sum_{i=1}^n L' \left( \frac{1 - X_i^T \mathbf{x}^{(t)}}{b_1} \right) K \left( \left\| \frac{z^{(t)} - Z_i}{b_2} \right\|_2 \right)^2} \\ \frac{\sum_{i=1}^n Z_i \cdot L' \left( \frac{1 - X_i^T \mathbf{x}^{(t)}}{b_1} \right) K' \left( \left\| \frac{z^{(t)} - Z_i}{b_2} \right\|_2 \right)^2}{\sum_{i=1}^n L' \left( \frac{1 - X_i^T \mathbf{x}^{(t)}}{b_1} \right) K' \left( \left\| \frac{z^{(t)} - Z_i}{b_2} \right\|_2 \right)^2} \end{pmatrix}, \quad (\text{B9})$$

given the Cartesian coordinates  $\{X_1, \dots, X_n\}$  of observations on  $\mathbb{S}^2$  and their redshift values  $\{Z_1, \dots, Z_n\}$ . The mean shift algorithm is guaranteed to converge to a local mode of the estimated density function for any initial point on  $\mathbb{S}^2$  or  $\mathbb{S}^2 \times \mathbb{R}$  if the smoothing bandwidth parameters are sufficiently small (Arias-Castro et al. 2016; Zhang & Chen 2021a).

• **Identifying knots.** We adopt the metric graph reconstruction algorithm (Aanjaneya et al. 2011; Lecci et al. 2014) from Appendix A in Chen et al. (2016) to identify the knots (or intersections) from a given set  $R$  of the filament. Specifically, the algorithm classifies each point  $\mathbf{y} \in R$  as ‘‘Knot’’ or ‘‘Non-Knot’’ as follows:

- (i) Subset those points on the filaments whose distance to  $\mathbf{y}$  is between  $r_{\text{in}}$  and  $r_{\text{out}}$ .
- (ii) Partition this subset of points via hierarchical clustering, where the clusters will not be merged if the average distance between these two clusters is above the threshold value  $r_{\text{sep}}$ .
- (iii) Count the number of clusters in the last step. If this number is greater or equal to three, we assign label ‘‘Knot’’ to  $\mathbf{y}$ . Otherwise,  $\mathbf{y}$  is a ‘‘Non-Knot’’ point.

We set the tuning parameters in the above procedures as:

- Spherical case :  $r_{\text{in}} = \frac{2b}{3}, \quad r_{\text{out}} = 2r_{\text{in}}, \quad r_{\text{sep}} = \frac{r_{\text{in}} + r_{\text{out}}}{2};$
- Conic case :  $r_{\text{in}} = \frac{2(b_1 + b_2)}{3}, \quad r_{\text{out}} = 2r_{\text{in}}, \quad r_{\text{sep}} = \frac{r_{\text{in}} + r_{\text{out}}}{2}.$

#### APPENDIX C: UNCERTAINTY MEASURE WITH (SMOOTHED) BOOTSTRAP METHOD

Besides detecting some valid filaments from discrete observations with our extended SCMS algorithms in SCONCE, we reveal the possibility of quantifying the uncertainty level of each filamentary point on the celestial sphere  $\mathbb{S}^2$  and 3D light cone  $\mathbb{S}^2 \times \mathbb{R}$  via the bootstrap technique (Efron 1979; Efron & Tibshirani 1994). As in Chen et al. (2015b), we consider both the nonparametric and smoothed bootstraps (Efron 1981; Silverman & Young 1987) under our extended SCMS algorithms in Section 2.2 and Section 2.3.

#### C1 Outline of the Bootstrap Procedure

Recall that our observational data sample is  $\mathcal{D} = \{U_1, \dots, U_n\}$ , where  $U_i = X_i \in \mathbb{S}^2$  for spherical data and  $U_i = (X_i, Z_i) \in \mathbb{S}^2 \times \mathbb{R}$  for conic data for  $i = 1, \dots, n$ . Notice that in Appendix B2, the stellar property  $Y_i$  for each observation  $X_i \in \mathbb{S}^2$  is an auxiliary variable assisting the filament detection, so the observational data  $U_i = (X_i, Y_i), i = 1, \dots, n$  in that scenario should also be treated as spherical data as well. At a high level, the bootstrap procedure of measuring the uncertainties on the estimated filaments  $\hat{R}$  consists of three main steps:

- (i) resample  $B$  different datasets from the original data sample,

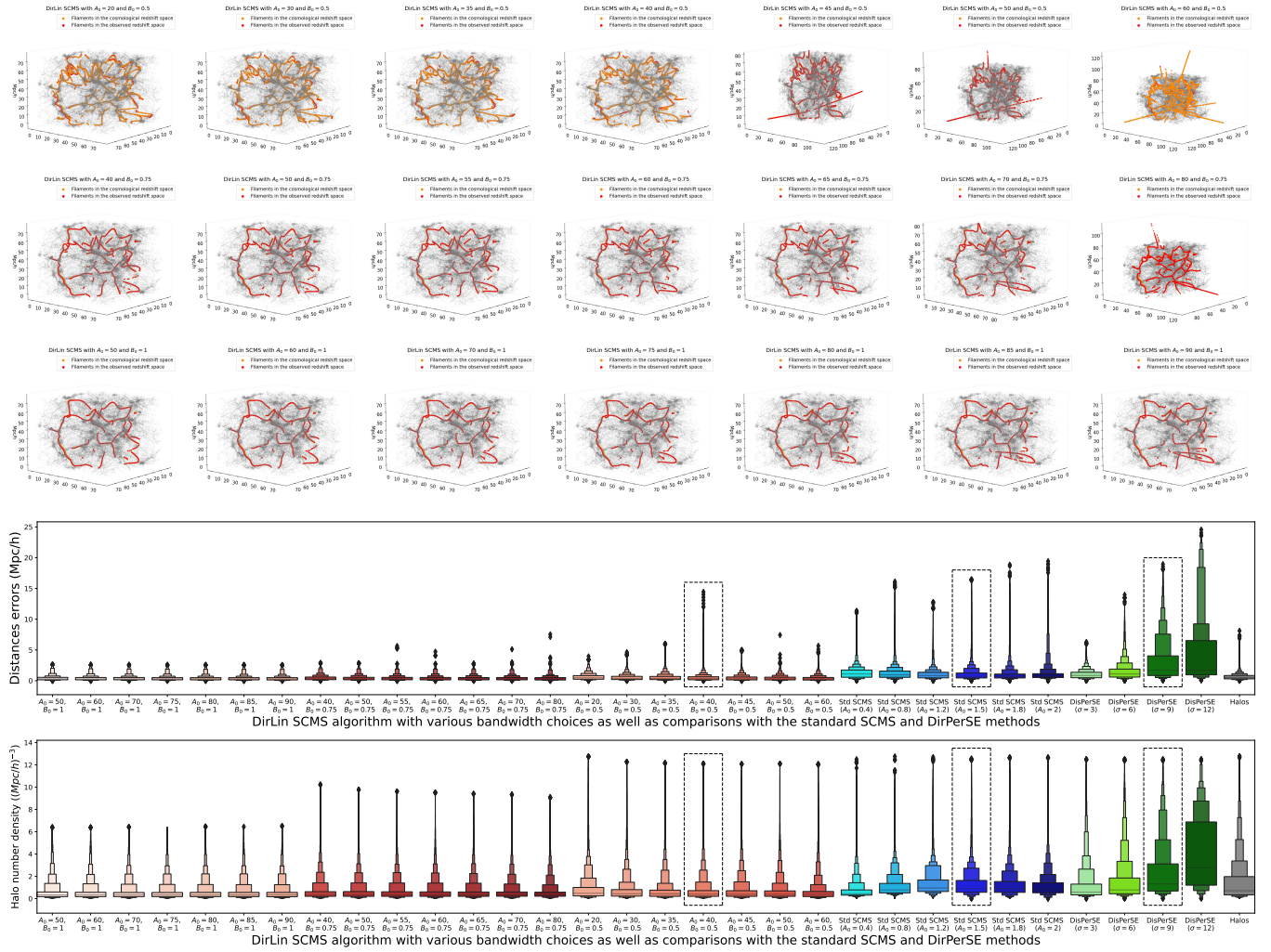


**Figure B2.** Comparisons of the filamentary structures detected by our DirLinSCMS algorithm in the observed and cosmological redshift spaces under different choices of the bandwidth parameters on the FoF halos of Illustris-3 at redshift  $z = 0$ . *Fourth Row:* The comparative letter-value plots of distance errors from the filaments detected by each method in the observed redshift space to the ones in the cosmological redshift space. *Fifth row:* The comparative letter-value plots of the halo number densities for the filamentary points detected by each method in the observed redshift space. At the fourth and fifth rows, the letter-value plots within dashed rectangles corresponds to the results in Figure 6.

- (ii) estimate the bootstrapped filaments  $\widehat{R}^{*(j)}$ ,  $j = 1, \dots, B$  on each resampled dataset via the DirSCMS algorithm on  $\mathbb{S}^2$  or DirLinSCMS algorithm on  $\mathbb{S}^2 \times \mathbb{R}$ , and
- (iii) measure the uncertainty of each point  $\mathbf{u} \in \widehat{R}$  as:

$$\rho(\mathbf{u}) = \sqrt{\frac{1}{B} \sum_{j=1}^B d_g(\mathbf{u}, \widehat{R}^{*(j)})^2}, \quad (\text{C1})$$

where  $d_g(\mathbf{u}, \widehat{R}^{*(j)}) = \min\{d_g(\mathbf{u}, \mathbf{u}^*) : \mathbf{u}^* \in \widehat{R}^{*(j)}\}$  for  $j = 1, \dots, B$ .

This framework of measuring the filamentary uncertainties is adopted from Chen et al. (2015b); Carrón Duque et al. (2022). The only difference is that we use the geodesic distance metric to calculate the distances from each point on the estimated filament  $\widehat{R}$  with the original data to the bootstrapped filaments  $\widehat{R}^{*(j)}$ ,  $j = 1, \dots, B$  as:

$$d_g(\mathbf{u}_1, \mathbf{u}_2) = \begin{cases} \arccos(\mathbf{u}_1^T \mathbf{u}_2) & \text{if } \mathbf{u}_i \in \mathbb{S}^2, \\ \|\mathbf{z}_1 \mathbf{x}_1 - \mathbf{z}_2 \mathbf{x}_2\|_2 & \text{if } \mathbf{u}_i = (\mathbf{x}_i, z_i) \in \mathbb{S}^2 \times \mathbb{R}, \end{cases} \quad (\text{C2})$$

for  $i = 1, 2$  so as to take into account the spherical or conic geometry.

## C2 Two Types of the Bootstrap Scheme

With regards to the bootstrap resampling mechanism, we consider two different versions available in the literature:

- **Nonparametric Bootstrap:** It was the very first bootstrap version initially proposed by Efron (1979), which has its own simplicity and is widely used in all scientific fields. Each bootstrap sample  $\{\mathbf{U}_1^{*(j)}, \dots, \mathbf{U}_n^{*(j)}\}$  with  $j = 1, \dots, B$  is sampled *with replacement* from the original data sample  $\mathcal{D} = \{\mathbf{U}_1, \dots, \mathbf{U}_n\}$ .

- **Smoothed Bootstrap:** It is a variant of the nonparametric bootstrap in which each bootstrap sample is generated not directly from the original data sample  $\mathcal{D}$  but from the estimated density function (c.f., Equations (5), (B2), or (8)). Given the original data sample  $\mathcal{D} = \{\mathbf{U}_1, \dots, \mathbf{U}_n\}$ , it repeats the following two-step process  $n$  times ( $i = 1, \dots, n$ ) in order to obtain one smoothed bootstrap data sample  $\{\mathbf{U}_1^{*(j)}, \dots, \mathbf{U}_n^{*(j)}\}$ :

- (i) We first sample a candidate point  $\tilde{U}$  uniformly from  $\mathcal{D}$ .
- (ii) Depending on the data type, we draw  $U_i^{*(j)}$  as follows:
- If  $\tilde{U} = \tilde{X} \in \mathbb{S}^2$ , sample  $X^*$  from the distribution with density  $\tilde{f}(x) = C_L(b) \cdot L\left(\frac{1-x^T \tilde{X}}{b^2}\right)$  and take  $U_i^{*(j)} = X^*$ .
  - If  $\tilde{U} = (\tilde{X}, \tilde{Z}) \in \mathbb{S}^2 \times \mathbb{R}$ , sample  $X^*$  from the distribution with density  $\tilde{f}_1(x) = C_L(b_1) \cdot L\left(\frac{1-x^T \tilde{X}}{b_1^2}\right)$  and  $Z^*$  from the distribution with density  $\tilde{f}_2(z) = \frac{1}{b_2} K\left(\left\|\frac{z-\tilde{Z}}{b_2}\right\|_2\right)$ . Then, take  $U_i^{*(j)} = (X^*, Z^*)$ .

Sampling data points from the above densities (or equivalently, some arbitrary kernel functions) could be difficult in practice. However, the problem can be resolved with our applications of the von Mises kernel  $L(r) = e^{-r}$  and Gaussian kernel  $K(r) = \frac{1}{\sqrt{2\pi}} e^{-\frac{r^2}{2}}$ . We discuss how to analytically sample  $X^*$  from  $\tilde{f}_1(x)$  on  $\mathbb{S}^2$  in Appendix C3, and sampling  $Z^*$  from  $\tilde{f}_2(z)$  is the same as adding Gaussian noise with mean 0 and variance  $\frac{1}{b_2^2}$ .

Compared to the smoothed bootstrap, the nonparametric bootstrap is more comprehensible and independent of the density function estimator. The smoothed bootstrap, on the other hand, requires a sampling scheme from the directional kernel function  $L$  in (5) (as well as the linear kernel function  $K$  in (8)) a priori, which may be computationally intensive for some kernel functions. Although one can always design a rejection sampling scheme (Flury 1990) to generate data points from any kernel function, the rejection sampling may be quite inefficient depending on the proposal density. Fortunately, we do have an analytic sampling approach for the von Mises kernel on  $\mathbb{S}^2$  and  $\mathbb{S}^2 \times \mathbb{R}$  in Appendix C3. Despite the complexity in its design, the smoothed bootstrap resolves the issue of only having (repeated) observations from the original data as in the nonparametric bootstrap and can reduce the mean squared error in the estimation of uncertainty measures under a proper choice of the smoothing bandwidth parameter (Silverman & Young 1987).

### C3 Analytic Sampling from the von Mises Kernel on $\mathbb{S}^2$

One interesting fact about the von Mises kernel  $L(r) = e^{-r}$  is that the resulting directional KDE (5) becomes a  $n$ -mixture of von-Mises Fisher (vMF) distribution on  $\mathbb{S}^2$ . The density function of a vMF distribution is defined as:

$$f_{\text{vMF}}(\mathbf{x}; \boldsymbol{\mu}, \kappa) = C_q(\kappa) \cdot \exp\left(\kappa \boldsymbol{\mu}^T \mathbf{x}\right) \quad (\text{C3})$$

with  $C_q(\kappa) = \frac{\kappa^{\frac{q-1}{2}}}{(2\pi)^{\frac{q+1}{2}} I_{\frac{q-1}{2}}(\kappa)}$ . Here,  $\boldsymbol{\mu} \in \mathbb{S}^2$  is the directional mean

of the vMF distribution,  $\kappa \geq 0$  is the concentration parameter, and

$$I_\alpha(\kappa) = \frac{\left(\frac{\kappa}{2}\right)^\alpha}{\pi^{\frac{1}{2}} \Gamma\left(\alpha + \frac{1}{2}\right)} \int_{-1}^1 (1-t^2)^{\alpha-\frac{1}{2}} \cdot e^{\kappa t} dt$$

is the modified Bessel function of the first kind of order  $\alpha$ , where  $\Gamma(\cdot)$  is the Gamma function. We denote this distribution by  $\text{vMF}(\boldsymbol{\mu}, \kappa)$ . Under this notation, the directional KDE (5) under the von Mises kernel  $L(r) = e^{-r}$  can be expressed as:

$$f(\mathbf{x}) = \frac{1}{n} \sum_{i=1}^n \text{vMF}\left(X_i, \frac{1}{b^2}\right),$$

and thus, sampling a data point from the density  $\tilde{f}(x) = C_L(b) \cdot L\left(\frac{1-x^T \tilde{X}}{b^2}\right)$  on  $\mathbb{S}^2$  in the smoothed bootstrap of Appendix C2 is equivalent to generating a random observation from  $\text{vMF}\left(\tilde{X}, \frac{1}{b^2}\right)$ .

Now, we illuminate an analytic approach to randomly sampling data points from a general  $\text{vMF}(\boldsymbol{\mu}, \kappa)$  on  $\mathbb{S}^2$ , which is far more efficient than the naive rejection sampling. We first consider generating  $X$  from  $\text{vMF}(\boldsymbol{\mu}_0, \kappa)$  with  $\boldsymbol{\mu}_0 = (0, 0, 1)^T \in \mathbb{S}^2 \subset \mathbb{R}^3$ . Based on the results in Ulrich (1984); Wood (1994); Kurz & Hanebeck (2015), we know that  $X$  follows  $\text{vMF}(\boldsymbol{\mu}_0, \kappa)$  if and only if

$$X = \left(\sqrt{1-W^2} \cdot U, W\right)^T,$$

where  $U$  is uniformly distributed on  $\mathbb{S}^1 = \{\mathbf{x} \in \mathbb{R}^2 : \|\mathbf{x}\|_2 = 1\}$  and  $W \in [-1, 1]$  has its probability density function as:

$$f_W(w) = \frac{\kappa}{e^\kappa - e^{-\kappa}} \cdot \exp(\kappa w) \quad \text{when } w \in [-1, 1], \quad (\text{C4})$$

whose corresponding cumulative distribution function (CDF) is

$$F_W(t) = \frac{e^{\kappa t} - e^{-\kappa}}{e^\kappa - e^{-\kappa}} \quad \text{when } t \in [-1, 1].$$

Some algebra show that the inverse of the above CDF is given by

$$F_W^{-1}(y) = \frac{1}{\kappa} \log \left[ y(e^\kappa - e^{-\kappa}) + e^{-\kappa} \right]. \quad (\text{C5})$$

To avoid numerical overflow for large values of  $\kappa$ , one can replace (C5) with the following equivalent expression

$$F_W^{-1}(y) = 1 + \frac{1}{\kappa} \log \left[ y + (1-y)e^{-2\kappa} \right]. \quad (\text{C6})$$

The random variable  $F_W^{-1}(Y)$  with  $Y \sim \text{Uniform}[0, 1]$  will have a density function (C4) and CDF (C5) or (C6). The sampling of  $U$  that is uniformly distributed on  $\mathbb{S}^1$  is relatively easy. For instance, one can sample  $U \sim \text{Uniform}[0, 1]$  and take  $U = (\cos 2\pi U, \sin 2\pi U)$ . Thus, the analytic strategy for sampling  $X \sim \text{vMF}(\boldsymbol{\mu}_0, \kappa)$  on  $\mathbb{S}^2$  is now clear.

To obtain data points from  $\text{vMF}(\boldsymbol{\mu}, \kappa)$  with an arbitrary mean direction  $\boldsymbol{\mu} \in \mathbb{S}^2$ , one can apply a rotation matrix  $R_{\text{rot}} \in \mathbb{R}^{3 \times 3}$  to the data sample from  $\text{vMF}(\boldsymbol{\mu}_0, \kappa)$ . One remarkable fact related to the expression of  $R_{\text{rot}}$  is that, in order to move a normalized vector  $\boldsymbol{\mu}_0 \in \mathbb{S}^2$  to another normalized vector  $\boldsymbol{\mu} \in \mathbb{S}^2$ , one only needs to rotate  $\boldsymbol{\mu}_0$  with respect to the axis  $\mathbf{k} = \frac{\boldsymbol{\mu}_0 + \boldsymbol{\mu}}{2}$  by the angle  $\pi$ . With the matrix form of the Rodrigues's rotation formula (Maritz 2021), one gets the beautiful formula for the rotation matrix as:

$$R_{\text{rot}} = 2 \frac{(\boldsymbol{\mu}_0 + \boldsymbol{\mu})(\boldsymbol{\mu}_0 + \boldsymbol{\mu})^T}{(\boldsymbol{\mu}_0 + \boldsymbol{\mu})^T (\boldsymbol{\mu}_0 + \boldsymbol{\mu})} - \mathbf{I}_3. \quad (\text{C7})$$

Note that this rotation matrix will indeed rotate the data point with respect to  $\boldsymbol{\mu}_0$  by the angle  $\pi$  when  $\boldsymbol{\mu}_0 = \boldsymbol{\mu}$ .

In short, the analytic algorithm for randomly sampling a data point  $X_{\text{vMF}} \sim \text{vMF}(\boldsymbol{\mu}, \kappa)$  with  $\boldsymbol{\mu} \in \mathbb{S}^2$  is given by

(i) Sample two independent data points  $Y$  and  $U$  from  $\text{Uniform}[0, 1]$ .

(ii) Compute  $W = 1 + \frac{1}{\kappa} \log \left[ Y + (1-Y)e^{-2\kappa} \right]$  and  $U = (\cos 2\pi U, \sin 2\pi U)$ .

(iii) Obtain  $X = \left(\sqrt{1-W^2}U, W\right)^T$  and rotate it as  $X_{\text{vMF}} = R_{\text{rot}}X$ .

This efficient sampling scheme will be applied to our smoothed bootstrap procedure in Appendix C2 when we deal with astronomical observations on  $\mathbb{S}^2$  or  $\mathbb{S}^2 \times \mathbb{R}$ .

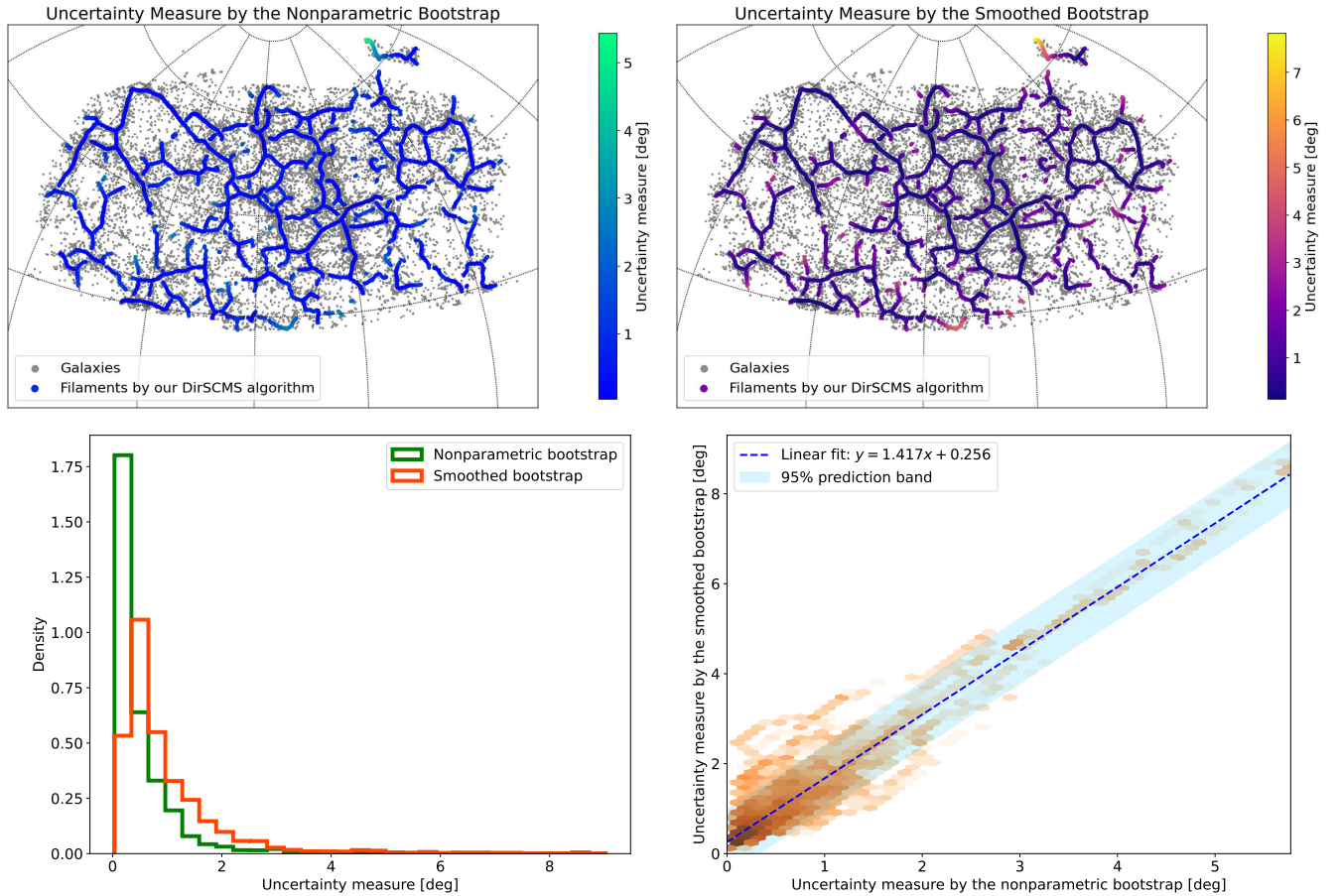


**Figure C1.** Comparisons of the uncertainty measures on the estimated filaments by the nonparametric and smoothed bootstraps with our `DirSCMS` algorithm on a thin redshift slice ( $0.06 \leq z < 0.065$ ) of the SDSS-IV galactic data. *Upper Row:* The cosmic filaments detected by our `DirSCMS` algorithm with their uncertainty measures by the two bootstrap methods. *Bottom Left:* Histograms of the uncertainty measures for the filaments by the two bootstrap methods. *Bottom Right:* The 2D histogram of the uncertainty measures for filamentary points by the two bootstrap methods, where the blue dashed line is a linear fit on the uncertainty measure data.

#### C4 Comparison between the nonparametric and smoothed bootstraps on SDSS data

We conduct a quantitative comparison between the nonparametric and smoothed bootstraps on  $\mathbb{S}^2$  by applying them to the SDSS-IV galactic data in Section 3.2 within the thin redshift slice  $0.06 \leq z < 0.065$  and the North Galactic Cap ( $100^\circ < \text{RA} < 270^\circ$ ,  $-5^\circ < \text{DEC} < 70^\circ$ ). The total number of galaxies is 26,919 in this spherical slice, including those with missing stellar masses by the FIREFLY model. Both the nonparametric and smoothed bootstrap procedures follow from the procedures in Appendix C1 with our `DirSCMS` algorithm and bootstrapping time  $B = 100$ .

The results are shown in Figure C1, where, on average, the smoothed bootstrap produces a higher value of the uncertainty measure for each point on the filament estimated by our `DirSCMS` algorithm than the nonparametric bootstrap. Nevertheless, the two bootstrap methods do not exhibit too much difference in quantifying the uncertainties on the estimated filament as a whole. Those points on the filament with high uncertainties by the nonparametric bootstrap are also less robust under the smoothed bootstrap. Indeed, as revealed by the bottom right panel of Figure C1, the uncertainty measures yielded by the nonparametric and smoothed bootstraps are linearly correlated with the Pearson’s correlation coefficient as 0.936. Hence, in the cosmic filament detection process, one can freely choose to use

either the nonparametric or smoothed bootstrap methods to measure the uncertainties of the estimated filaments, as long as the method is consistent along the entire filament detection pipeline.

This paper has been typeset from a  $\text{\TeX}/\text{\LaTeX}$  file prepared by the author.